國立臺灣大學理學院化學所

碩士論文

Department of Chemistry

College of Science

National Taiwan University

Master's Thesis

限制空間導引之氫氣生成反應

Confinement Induced Hydrogen Evolution Reaction

黃子軒

Tzu-Hsuan Huang

指導教授: 鄭修偉 博士

Advisor: Hsiu-Wei Cheng Ph.D.

中華民國 113 年 9 月

September, 2024

doi:10.6342/NTU202404416

國立臺灣大學碩士學位論文
口試委員會審定書
NTU Master Thesis
Oral Defense Approval Form

限制空間導引之氫氣生成反應

Confinement Induced Hydrogen Evolution Reaction

本論文係 黃子軒 君（學號 R11223191）在國立臺灣大學化學系完成之碩士學位論文，於民國 113 年 9 月 10 日承下列考試委員審查通過及口試及格，特此證明。

The student Tzu-Hsuan Huang (student no. R11223191) enrolled in the Master Program of the Department of Chemistry, NTU has satisfactorily passed the oral defense on 2024/09/10 with the approval of all committee members as follows.

口試委員(Committee Members)：

劉俊彥 （簽名 Signature）

（指導教授 Advisor）

陳逸聖　　陳俊顯

簡儀珏

系主任、所長 陳振中 （簽章）

(Dept./Institute Chair's Signature and Seal)

doi:10.6342/NTU202404416

Acknowledgements

I would like to express my deepest gratitude to several individuals whose support and guidance have been instrumental in the completion of my thesis.

First and foremost, I would like to thank my professor, Dr. Hsiu-Wei Cheng, for his invaluable guidance and support throughout my research. His enthusiasm for design and assembly has inspired me, and his willingness to share his thoughts on experimental results has helped me develop critical thinking skills essential for my research.

I am also deeply grateful to Valentina Wieser, the senior PhD student who mentored me. She taught me the operational principles and procedures of the Surface Force Apparatus (SFA), and meticulously reviewed my thesis, providing numerous suggestions for improvement. Her patience, insights, and constant encouragement have been a source of inspiration and motivation.

A special thank you goes to Dominik Dworschak from Forschungszentrum Jülich GmbH, Helmholtz Institute Erlangen-Nürnberg for Renewable Energy, the visiting post-doctoral researcher. Our discussions about my research progress were invaluable, and he was always willing to offer his perspectives and suggestions. His constructive feedback and collaborative spirit have significantly enriched my research experience.

I would also like to thank my colleagues, friends, and family. Their unwavering

doi:10.6342/NTU202404416

support, whether through lending an ear or providing moral support, has been crucial in helping me stay focused and motivated throughout this journey. I am deeply grateful for their presence in my life.

Most importantly, I want to thank my girlfriend, Bblythe Lee, for her patience and understanding. While I spent countless hours working on my thesis, she stood by me and offered unwavering support, even when I couldn't spend much time with her. Her love and encouragement have been a constant source of strength.

Thank you all for your contributions and support.

doi:10.6342/NTU202404416

摘要

氫氣是重要的乾淨能源，電解水為產生氫氣的方法之一，目前大多數研究集中在通過合成新材料或改變材料表面化學組成來尋找能取代貴金屬的高效氫氣生成反應 (Hydrogen Evolution Reaction, HER) 的電催化劑而我們則探索了通過改變材料的幾何結構來提高催化性能。我們利用表面力儀（Surface Force Apparatus, SFA）在金和雲母表面之間創建奈米至微米級的限制空間，觀察並分析在此條件下導引的 HER 催化現象。通過遷移、對流和擴散等機制來研究水合氫離子在限制空間中的質量傳輸過程，並使用 Comsol 多物理場建模和原位影像分析等方法來深入理解這些作用。研究顯示，限制空間會提高電極表面電位並促使水合氫離子遷移。氣泡的形成會撐開限制空間，提供水合氫離子運輸通道並引發微對流，加速電解質進入間隙。雲母表面的高水合氫離子濃度使水合氫離子從雙電層擴散到金表面，增強水合氫離子傳輸。但這些短程作用無法完全解釋催化能力，暗示存在長程相互作用。本研究證明，通過改變材料的幾何結構而非表面組成，可以有效提升 HER 催化性能，並以質量傳輸的角度為此現象提供了解釋。

關鍵字：氫氣生成反應、限制空間、電催化、干涉光學

doi:10.6342/NTU202404416

doi:10.6342/NTU202404416

Abstract

Hydrogen is an important clean energy source, and water electrolysis is one of the methods for producing hydrogen. Currently, most research focuses on finding efficient electrocatalysts for the hydrogen evolution reaction (HER) that can replace precious metals by synthesizing new materials or altering the chemical composition of material surfaces. In our study, we explored enhancing catalytic performance by changing the geometric structure of the materials. We used a Surface Force Apparatus (SFA) to create nanometer to micrometer-scale confined spaces between gold and mica surfaces, observing and analyzing the HER catalytic phenomena under these conditions. We investigated the mass transport processes of hydronium ion in confined spaces through mechanisms such as migration, convection, and diffusion, and used Comsol multiphysics modeling and in-situ imaging analysis to gain a deeper understanding of these effects. Our research showed that confined spaces increase the electrode surface potential and promote the migration of hydronium ion. The formation of bubbles expands the confined spaces, pro-

doi:10.6342/NTU202404416

viding channels for the transport of hydronium ion and inducing micro-convection, which accelerates the entry of electrolytes into the gaps. The high concentration of hydronium ion on the mica surface enhances the diffusion of these ions from the electric double layer of mica to the gold surface, improving ion transport. However, these short-range effects do not fully explain the catalytic capability, suggesting the presence of long-range interactions. This study demonstrates that altering the geometric structure of materials, rather than their surface composition, can effectively enhance HER catalytic performance, providing an explanation for this phenomenon from the perspective of mass transport.

Keywords: Hydrogen evolution reaction, Confined space, Electrocatalyst, Interferometry

doi:10.6342/NTU202404416

Contents

doi:10.6342/NTU202404416

doi:10.6342/NTU202404416

doi:10.6342/NTU202404416

doi:10.6342/NTU202404416

List of Figures

doi:10.6342/NTU202404416

doi:10.6342/NTU202404416

doi:10.6342/NTU202404416

doi:10.6342/NTU202404416

doi:10.6342/NTU202404416

doi:10.6342/NTU202404416

List of Tables

doi:10.6342/NTU202404416

doi:10.6342/NTU202404416

Denotation

A	Area (cm^2) of the working electrode
A_m	Amplitude of the electromagnetic wave
A_{contour}	Area of the contour
A_{rect}	Area of the smallest rectangle that can surround the contour
α_a	Charge transfer coefficient for the reaction at the anode
α_c	Charge transfer coefficient for the reaction at the cathode
CCD	Charge-Coupled Device
CE	Counter El2ectrode
C_i	The concentration of species i
c_i^o	The initial concentration of the redox species i
DLVO	Derjaguin-Landau-Verwey-Overbeek
d_{sep}	Separation distance

doi:10.6342/NTU202404416

D_i	The diffusion coefficient of species i
$E_{\text{Ag/AgCl}}$	The measured potential relative to the Ag/AgCl reference electrode
$E_{\text{Ag/AgCl, standard}}$	The standard potential of the Ag/AgCl electrode relative to SHE
$E_{applied}$	Applied potential
$E_{equilibrium}$	Thermodynamic equilibrium potential
E_{RHE}	Potential relative to the Reversible Hydrogen Electrode
ϵ	The permittivity of the electrolyte
η	Overpotential
η_{act}	Activation overpotential
η_{conc}	Concentration overpotential
η_{ohm}	Ohmic overpotential
FECO	Fringes of Equal Chromatic Order
F	Faraday constant
FPS	Frames per second
GEEs	Gas-Evolving Electrodes
HER	Hydrogen Evolution Reaction
I	The ionic strength

doi:10.6342/NTU202404416

i	Currents
J	Current density
J_0	Exchange current density
$\mathbf{J}_i$	The mass transport flux of species i
k	The wavenumber of an electromagnetic wave
k_b	Boltzmann constant
κ	The reciprocal of the Debye length
LSV	Linear Sweep Voltammetry
λ	The wavelength of an electromagnetic wave
λ_D	Debye length
MBI	Multiple Beam Interferometry
MS	Magnetron sputtering
μ_i	The mobility of species i
n	The order of interference
n_0	The number density of the electrolyte
n_{liquid}	The refractive index for one specific liquid
n_{mica}	The refractive index for mica

doi:10.6342/NTU202404416

N_A	Avogadro's number
NR	Newton Ring
OCP	Open Circuit Potential
PDEs	Partial Differential Equations
PVD	Physical Vapor Deposition
ψ	Electric potential
$\psi(x)$	The electric potential at x position
ψ_s	Surface potential
RE	Reference Electrode
RHE	Reversible Hydrogen Electrode
ROI	Regions Of Interest
R_g	Gas constant
S	Simmons
SFA	Surface Force Apparatus
s	Seconds
σ	Electrolyte conductivity
σ_s	Surface charge

doi:10.6342/NTU202404416

ρ	Charge density
ρ_0	Charge density of the bulk solution
T_{emp}	Absolute Temperature
TSM	Template Stripping Method
t	Time
θ	Surface coverage
θ_b	Bubble coverage
V	Volts
$\mathbf{v}$	The velocity of the bulk fluid
WE	Working Electrode
z_i	The charge of species i

doi:10.6342/NTU202404416

doi:10.6342/NTU202404416

Chapter 1 Introduction

1.1 Hydrogen evolution reaction

Owing to the deficiency of clean energy, finding a new alternative to clean energy is getting increasingly urgent. Hydrogen is one of the cleanest sources of energy in the world.[1] It will only generate water after burning. Another advantage of hydrogen energy is that it can supply almost the biggest amount of energy per gram compared to other common fossil fuels.[2]

There are several ways to produce hydrogen gas; one way is by electrolysis of water, and the anode and cathode will generate oxygen and hydrogen, respectively, which is called Oxygen Evolution Reaction (OER) and Hydrogen Evolution Reaction (HER)[3].

The issue that green energy faces is that the peak time of electricity generation does not perfectly match the peak time of electricity usage. For example, solar panels can convert large amounts of solar energy to electricity energy during the daytime. However, the peak time for electricity usage is usually at night for family usage. This discrepancy causes the waste of an excess amount of electricity in the daytime and a power shortage at night for solar panels. Therefore, a way to convert and store the excess amount of energy is crucial, and one way to store the energy is to use the hydrogen gas as an energy warehouse.

doi:10.6342/NTU202404416

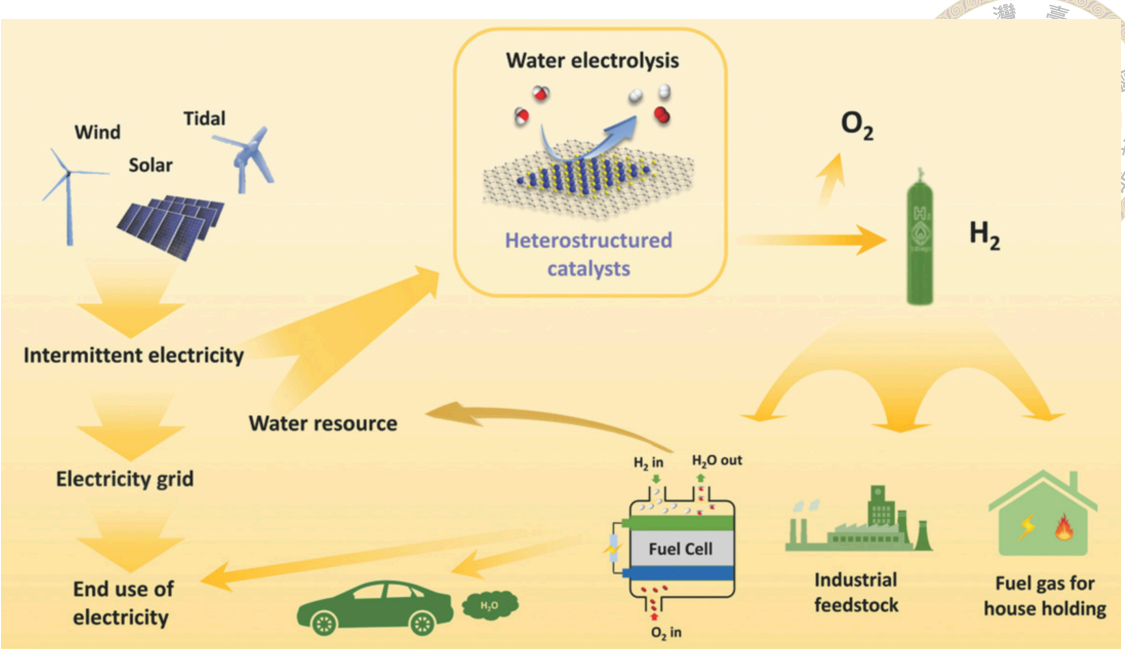

Figure 1.1: A sustainable pathway for the production and utilization of hydrogen energy .

There are several other advantages to using hydrogen besides energy storage as outlined in Figure 1.1[4]. All these mentioned applications highlight that hydrogen is very important in different areas such as fuel production, energy storage, and serving as industrious material. The importance of HER has been at the center of material science and the energy industry for centuries and is still a topic of new development and research for many scientists worldwide.

1.1.1 Mechanism of HER

Since we focus on the electrolysis of water, it is crucial to understand the mechanism of electrolytic water splitting, especially for the cathode reaction, HER. The mechanism of HER is affected by the electrolyte pH environment in the electrolyzer. In this thesis, we only discuss the mechanism in acid conditions. In acidic conditions, the hydronium ion first undergoes discharge and chemically adsorbs onto the electrode surface, a process known as the Volmer reaction. The second step can occur through two possible pathways:

doi:10.6342/NTU202404416

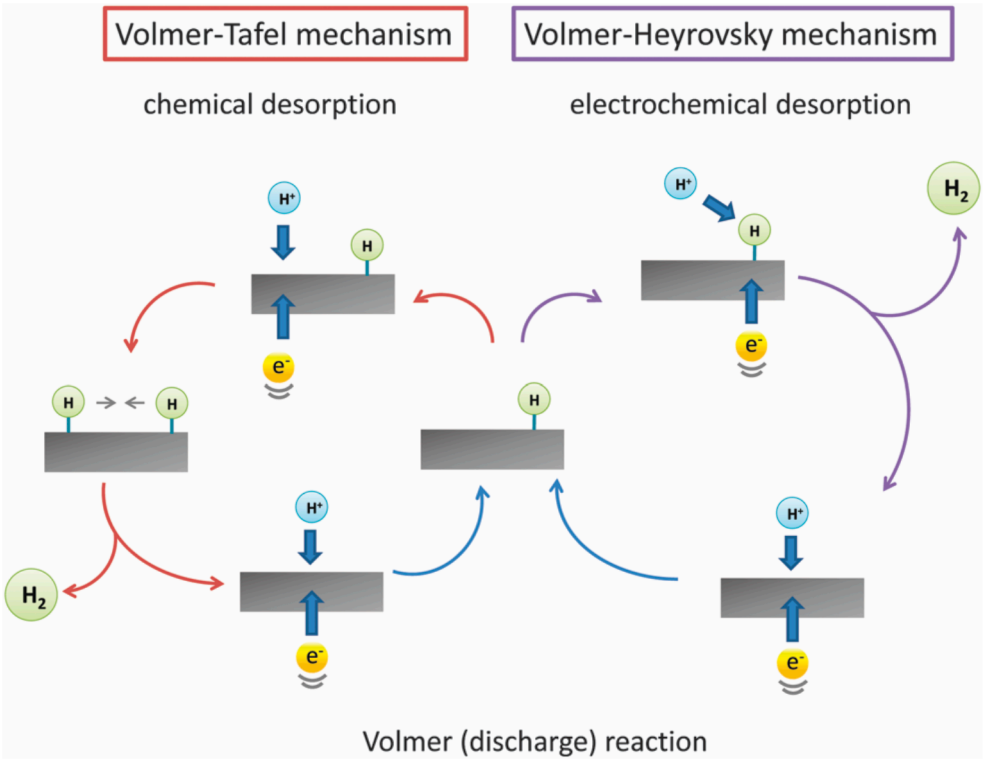

Figure 1.2: The mechanism of HER in acidic condition

the adsorbed proton (M-H) can either react with the proton in the solution and form molecular hydrogen, or two binding protons on the electrode in close proximity can couple with each other and form molecular hydrogen. The former is called the Heyrovsky reaction, while the latter is called the Tafel reaction.

As a result, we can see from Figure 1.2[5] that the reaction pathway can be categorized in two ways: the Volmer-Heyrovsky pathway and the Volmer-Tafel pathway. The determining factor for which pathway the electrode follows is the surface coverage (θ) of hydrogen atoms that have chemisorbed onto the electrode surface[6]

1.1.2 Overpotential of HER

The standard reduction potential for water splitting is 1.23 Volts. However, we usually need a higher potential to make the water start to split and generate hydrogen and

doi:10.6342/NTU202404416

oxygen.

This excess potential means the reaction needs more energy to overcome the energy barrier, and the excess energy that is consumed during the reaction will usually be emitted as wasted heat. We will describe the potential in excess of the thermodynamic equilibrium potential as overpotential (η).[7]. The equation of overpotential can be seen in Equation 1.1, which describes that the overpotential is equal to applied potential minus thermodynamic equilibrium potential.

$$\eta = E_{\text{applied}} - E_{\text{equilibrium}} \tag{1.1}$$

The energy waste due to overpotential is the present obstacle to applying hydrogen energy in commercial usage. Consequently, scientists are making progress in reducing the overpotential needed to initiate the reaction of the generation of molecular hydrogen.

One way to define the reaction as ”initiated” or ”started” to generate hydrogen is by discussing the current density transport through the electrode. It is well-accepted that we can use the value of 10 mA per centimeter square[8] as a standard value. We usually compare the overpotential that is needed to achieve a current density of 10 mA/cm^2; usually, the smaller value of this particular overpotential means the higher catalytic activity the material possesses

The common way of decreasing the overpotential of HER is by electrocatalyst, which uses some electrode material to faster the reaction rate on the electrode surface by changing the reaction mechanism, providing more active sites on the electrode, and so on.

doi:10.6342/NTU202404416

1.1.3 Electrocatalyst for HER

When describing the performance of an electrocatalyst for HER, one simple way is to have a look at the volcano plot. According to the Sabatier principle, an excellent electrocatalyst for HER has to form a suitable intermediate M-H, whose binding energy is neither too strong nor too weak.[9] If the binding energy of M-H is too weak, then the reactant can't adsorb to the electrode surface, but if the binding energy is too strong, then the intermediate won't be able to react further and detach from the electrode surface.

If we plot the exchange current density in logarithm scale versus bond energy between metal and hydrogen atom, we can get the volcano plot shown in Figure 1.3[10]. From Figure 1.3[10], we can find that noble metals such as Platinum exhibit relatively high current density, which is because the M-H bond strength is not too strong nor too weak, making noble metals the most efficient electrocatalysts toward HER.[11] However, precious metals are usually costly, and their production is often in a way that is harmful to the mining area[12]. Therefore, it is essential to find other alternative electrocatalytic materials for HER.

The current approach uses transition metals as the alternative electrocatalyst for HER and tries to alter the physical or chemical properties so that the selected catalyst can have a closer location on the volcano plot, close to where the precious metal is located, the peak of the volcano.

The intrinsic catalytic properties of transition metals are typically modified through surface alterations [13] or by using complex synthesis methods [14], which can change their electronic structures and enhance electrocatalytic activity.

doi:10.6342/NTU202404416

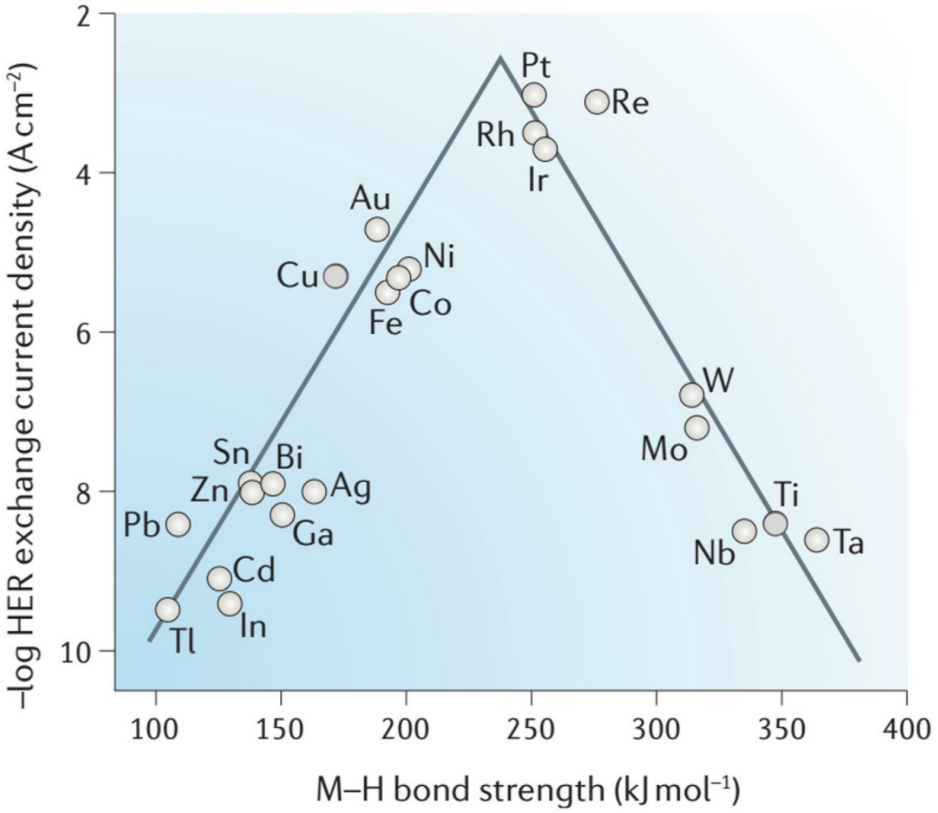

Figure 1.3: The volcano plot of commonly used metal material for hydrogen evolution reaction

1.2 Geometry effect

As discussed at the end of subsection 1.1.3, we aim to modify the intrinsic properties of common materials to develop cost-effective and efficient electrocatalysts for HER. Experimental methods such as surface doping[15], creating vacancies[16], and changing lattice strain[17] can reach our goal and enhance catalytic activity.

However, the process of altering the catalytic ability is usually time-consuming, which keeps us thinking about whether there is any other way to simplify the surface modification approach or even not do any kind of surface modification. We hope to only change the geometry of some very general materials and turn it into a high-performance HER electrocatalyst.

doi:10.6342/NTU202404416

Research conducted by Huang *et. al.* demonstrates that an array-patterned platinum nanostructure can effectively generate hydrogen by optimizing the distance between the platinum nanoparticles[18]. The author tunes the annealing temperature of platinum nanoparticles, resulting in different separation distances between Pt nanoparticles. The result in Figure 1.4[18]-(b)(c) shows that the separation distance between Pt atoms affects the catalytic ability parameters such as overpotential, turnover frequency, and specific current at 60 mV overpotential normalized by mass. The author explained that it is because when the separation distance is too small, the Tafel mechanism would be changed from inter-particle to intra-particle pathway, which accelerates the reaction rate. Inspired by this work, we became curious about two questions:

1. How does the separation distance affect the catalytic ability of electrodes?

2. Can we enhance the catalytic performance of an electrode simply by altering the surface geometry (separation distance) rather than by the surface modification method or by the complicated synthesis procedure?

In order to establish a well-defined separation distance between two surfaces to solve the questions above, we choose the Surface Force Apparatus (SFA) (details are in section 2.2) to do further experiments since SFA can control the separation distance between two surfaces in nanometer resolution. When the two surfaces reach a close proximity, the light penetrating through the system will construct an interference pattern called Newton Ring (NR). If the NR is cut by a slit and sent to a spectrometer, we can get the fringes of equal chromatic order (FECO), the FECO can be further analyzed (details are in subsection 2.2.2) and get the nano-meter-resolved separation distance between two surfaces.

doi:10.6342/NTU202404416

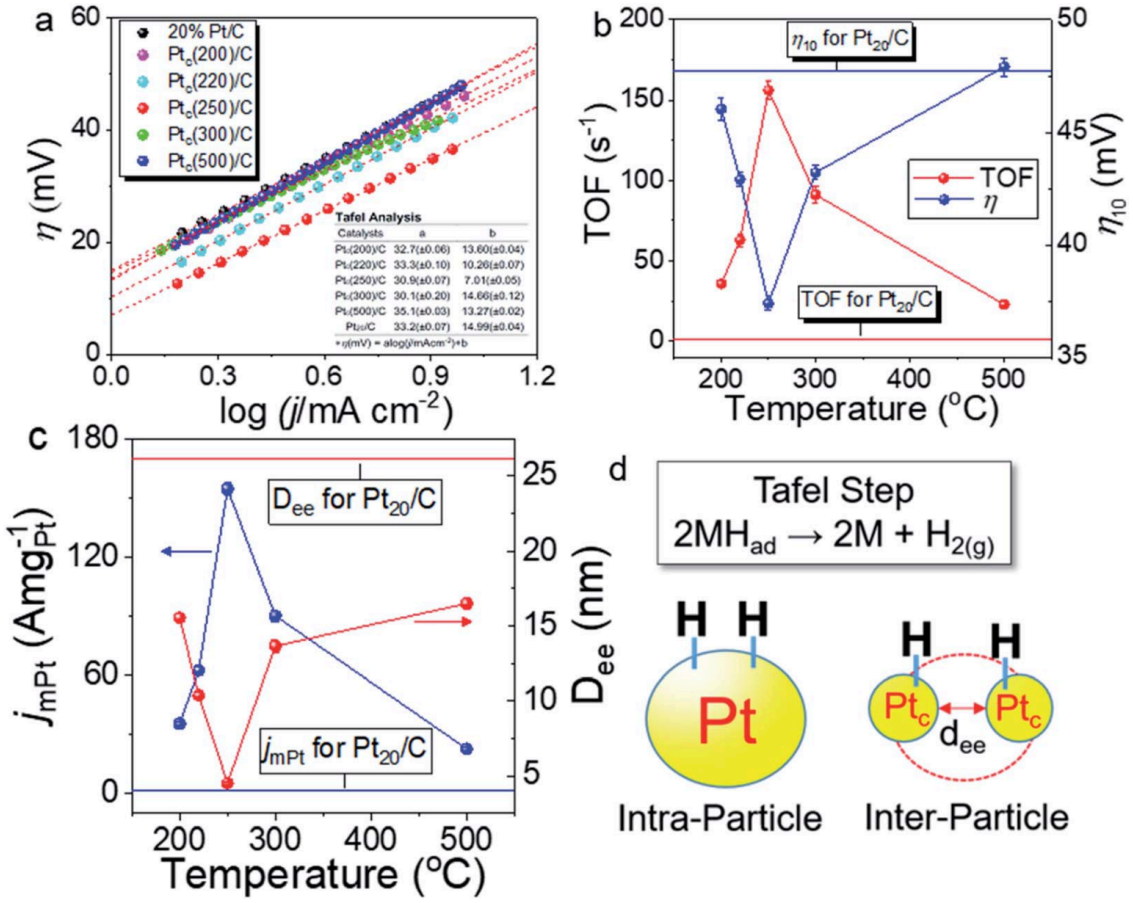

Figure 1.4: (a) The tafel slope of Pt after different thermal treatment temperatures. And the thermal treatment temperature versus (b) Turnover frequency (TOF) and overpotential (η), (c) specific current at a given overpotential normalized by mass and separation distance (D_{ee}) between two Pt nanoparticles (d) the schematic diagram of inter- and intra-particle tafel step

doi:10.6342/NTU202404416

1.3 Gas evolving electrodes

The HER reaction will generate a large number of hydrogen bubbles on the working electrode (WE) surface, and the bubbles will highly affect the HER reaction to proceed since it makes the electrode surface become a three-phase intersection rather than the traditional two-phase one (reactant in the solution react on the electrode surface). As a result, before we start to discuss the catalytic behavior on the electrode surface, we should introduce the concept of gas-evolving electrodes (GEEs) and explain what is the difference between GEEs compared with other electrodes that undergo homogeneous red-ox reaction and how GEEs affect the overpotential of HER.

Gas-evolving electrodes (GEEs) are described as gas evolution reactions that happen on the electrode surface. For typical GEEs, there are several aspects that are different from a homogeneous re-dox reaction electrode, such as the enhancement of the ohmic resistance due to the adhesion bubbles on the WE[19], increasing the mass transport effect by stirring the electrolyte near electrode surface[20], and so on. The bubbles generated from GEEs usually increase the overpotential of the reaction on the electrode. As a result, the discussion of bubble growth/detachment kinetic would be greatly important for the GEEs.

Since the geometry setup of SFA will make the two surfaces come very close, we found that the bubble formation behavior on the electrode surface is quite different from the traditional planar surface and further affects the catalytic ability in this confinement geometry. Consequently, it is important to introduce GEEs, bubble formation mechanisms, and overpotential results from bubbles.

doi:10.6342/NTU202404416

1.3.1 Bubble generation mechanism

Bubble evolution from the electrode surface usually contains three steps: nucleation, growth, and detachment[21]. Take the hydrogen evolution reaction, for example; when the potential is negative enough to produce hydrogen gas, the gas will first dissolve into the solution. After the solution near the electrode surface is super-saturated with hydrogen, the hydrogen gas starts to nucleate on the electrode surface, especially close to defects on the surfaces. After the nucleation, tiny bubbles will grow by adding hydrogen. When two or more larger bubbles reach close proximity, they will coalesce into one single bubble, enlarging the volume further. The growth of the bubble size will also increase the buoyancy of the bubble. After the buoyancy is larger than the adhesion force between the bubble and the electrode, it will detach from the electrode surface; this step is called detachment. The detachment of bubbles will also stir the electrolyte near the electrode surface, increasing the mass transport of the electrolyte. The above three steps of nucleation, growth, and detachment cycle are visualized in the schematic diagram in Figure 1.5[22].

1.3.2 Overpotential induced by bubbles on GEEs

The overpotential of GEEs can be highly affected by bubbles, which can be sorted into three kinds of overpotentials that are related to bubbles.

1. activation overpotential, η_{act}: governed by the bubble coverage on the surface
2. ohmic overpotential, η_{ohm}: related to bubble layer thickness on the electrode
3. concentration overpotential, η_{conc}: related to the micro convection when bubbles detach from the surface [21]

doi:10.6342/NTU202404416

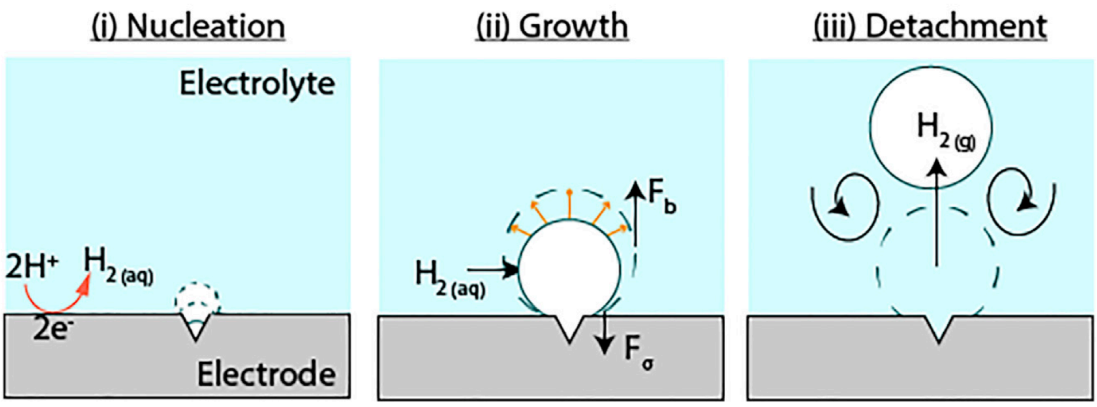

Figure 1.5: The evolution of bubbles on a GEE surface involves three main processes: (i) Nucleation, (ii) Growth, and (iii) Detachment. Nucleation generally occurs at the surface defects like cracks and pits. After the nucleation, the bubble grows by drawing in gas from the surrounding dissolved gas layer. Bubble detachment happens when the buoyant force surpasses the surface adhesion force, leading to the bubble detaching from the surface. The detachment of the bubble creates micro-convection near the electrode, which is indicated by the spiral curves.

To combine all these effects, we can write the overpotential arising from bubbles on GEEs in Equation 1.2 as:

$$\eta = \eta_{act} + \eta_{ohm} + \eta_{con} \tag{1.2}$$

η_{act} can be defined with Equation 1.3[23]:

$$\eta_{act} = \frac{R_g T_{emp}}{F} \ln \frac{1}{1-\theta_b} \tag{1.3}$$

where R_g is the gas constant, T_{emp} is the absolute temperature, F is the Faraday constant, and θ_b is the bubble coverage on the surface. This overpotential encompasses the fact that when the bubble is attached to the electrode surface, it blocks the active sites of the electrode, which induces energy loss when conducting an electrocatalytic reaction, and that is why the equation indicates that the η_{act} shows high correlation with bubble coverage. From the equation, we can infer that if we want to reduce η_{act}, the most crucial factor

doi:10.6342/NTU202404416

we need to control is the bubble coverage on the surface[24] as it is highly related to the bubble size and surface wettability.[25, 26]

Iwata et al. revealed how bubble coverage and bubble layer thickness affect bubble overpotential [27]. They first coated polytetrafluoroethylene (PTFE) on a nickel porous electrode at different coating coverages. As the coating coverage increased, the electrode became increasingly aerophilic. They found that a slight change in aerophilicity caused the bubble dynamics to exhibit three distinct modes. The relationship between PTFE coating coverage, bubble growth and departure mode, and bubble coverage is listed in Table 1.1.

PTFE coverage	0	0.16	0.55	0.76
Mode	Internal growth and departure	Wicking	Gas-filled	
Bubble coverage	0.001	0.35	0.4	0.47

Table 1.1: The relation between PTFE coating coverage, bubble growth and departure mode, and bubble coverage

The three modes are as follows:

- Internal Growth: When there's no PTFE coating, the electrode is intrinsically aerophobic. Therefore, the bubble departure radius is small and even smaller than the pore size, so the bubbles depart from both electrode surfaces and within the electrode.

- Wicking: The electrode becomes a little aerophilic, which enlarges the bubble departure size. The enlargement suppresses the number of bubbles that depart from the inner of the electrode.

- Gas-filled: The departure bubble size is larger than the pore size, which means the bubbles only depart from the electrode surface. However, the bubbles will coalesce within the pores and enlarge the bubble size.

doi:10.6342/NTU202404416

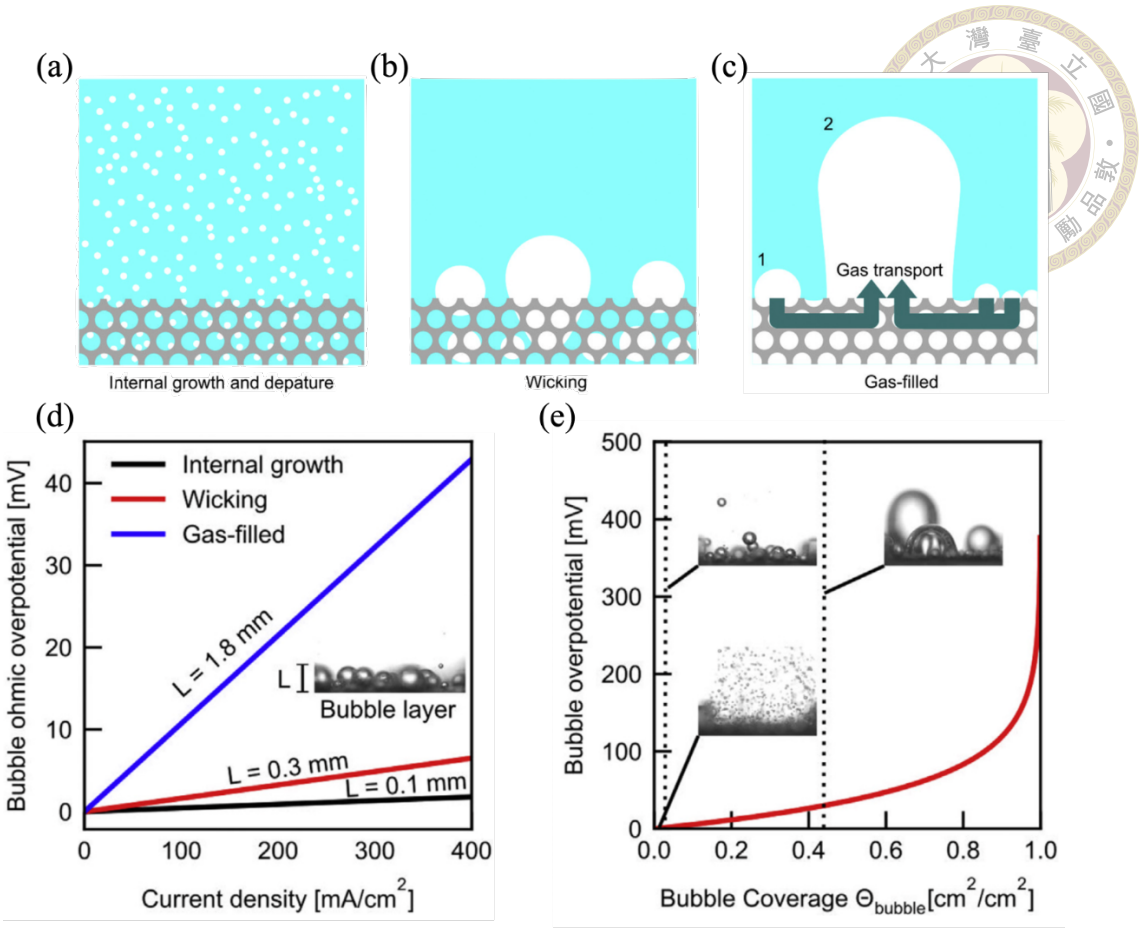

Figure 1.6: (Schematic illustration of different modes when bubbles are evolving from the porous Nickel electrode is shown in (a) to (c) (d) demonstrate the bubble ohmic overpotential as a function of current density for different bubble growth and detachment modes, as well as bubble layer thickness (L). The inset exhibits the side view image of bubbles within the bubble layer. (e) exhibit the bubble activation overpotential as a function of the bubble coverage. The inset demonstrates the side view images of the bubbles during different modes.

The schematic diagram of three modes is shown in the Figure 1.6[27] (a)-(c).

As we can see in Figure 1.6[27]-(e), Iwata et al. plots the relation between activation overpotential (η_{act}) and bubble surface coverage (θ_b) according to the formula shown in Equation 1.3, and label the coverage which corresponds to the three modes. We can find that the bubble overpotential indeed highly affects the overpotential of GEEs and is it is controlled by surface wettability and bubble departure size.

Bubble ohmic overpotential (η_{ohm}) describes the overpotential that is provoked by the attached bubbles on the electrode surface[28]. When the bubble layer on the electrode gets

doi:10.6342/NTU202404416

thicker, the ohmic overpotential will enlarge because the ion transporting pathway gets blocked by the bubble layer more severely. From Figure 1.6-(d), the author measures the bubble layer thickness of the three modes and calculates the relation between bubble ohmic overpotential and current density under such bubble layer thickness. From Figure 1.6[27]-(d). We know that if the bubble layer thickness increases, it also increases the bubble ohmic overpotential (η_{ohm}) [22].

When the bubble is large enough, it lifts off the electrode surface by the buoyancy. The surrounding electrolyte overwhelms the empty space that the bubble originally occupied, creating micro convection [29]. The micro convection phenomena greatly reduce the concentration overpotential (η_{conc}) to a relatively low value, and it also increases the electrolyte supplement during the reaction. However, the value of η_{conc} is negligible compared with the other two overpotentials, which is why we can neglect it in the following discussions.

1.4 Motivation and aims

Our group utilized Surface Force Apparatus (SFA) to produce confinement between the mica and gold surface. It was found that confinement can trigger HER near the confined area when negative polarization on the electrode is applied under lower overpotential conditions compared with free space (data will not show here). The observation of this phenomenon provoked a further investigation into the reasons and mechanism of this confinement-induced process .

We originally hypothesized that the geometry of the SFA, which confines the reaction area to a few nanometers, would make it more difficult for the reactant to enter the nano-

doi:10.6342/NTU202404416

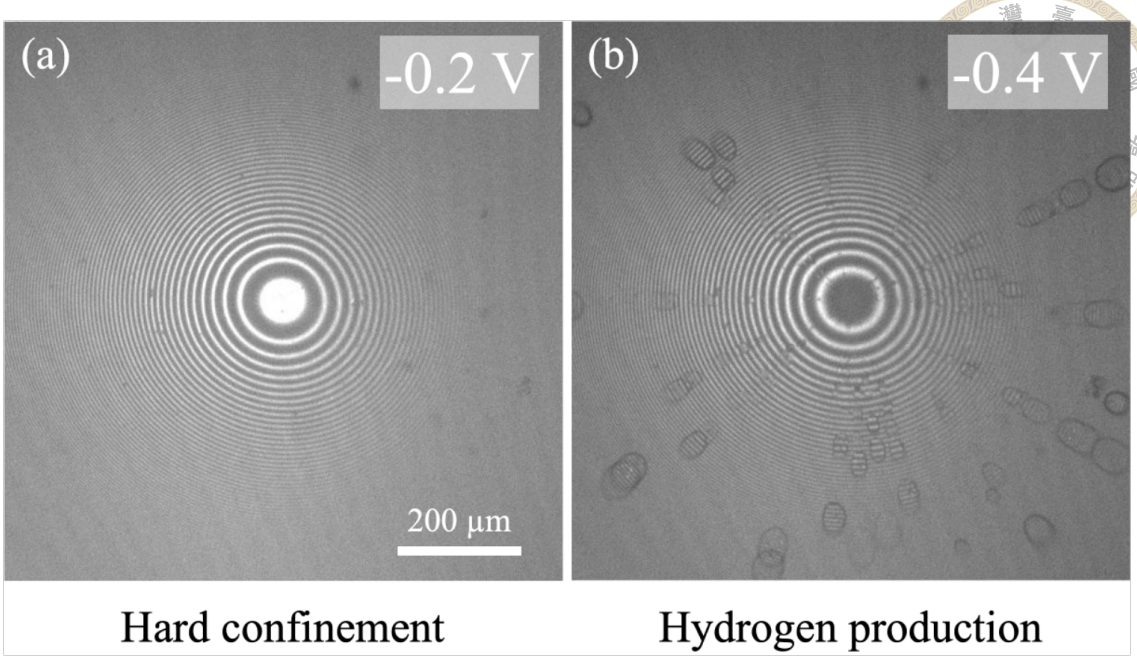

Figure 1.7: Top view of the WE surface under hard compression at different overpotentials, (a) no hydrogen generation on the working electrode under low overpotential, (b) hydrogen production at the confined area under high overpotential. The electrolyte is 0.5 M sulfuric acid. The light-dark alternative pattern is the Newton Ring, which is the interference pattern when the light penetrates through two semi-transparent mirrors, and multi-reflection constructs the interference pattern.

slit, thus hindering mass transport and requiring a higher overpotential for the reaction to proceed compared to unconfined space. Consequently, we expected that the confinement would reduce the HER reaction rate. However, the experimental results were completely contrary to this initial hypothesis. Due to this paradox, we focused on investigating how the reactant is transported into the confined region and addressing the key questions arising from this phenomenon. When discussing the mass transport flux of a given electrochemical reaction, three key factors dominate: diffusion, migration, and convection. In this thesis, we aim to resolve the question posed above by exploring these three factors within the confined region, where the conditions differ significantly from those in free space.

Despite the mass transport problem, we are also curious about whether the reaction is triggered through confinement itself or confinement between gold and mica. In other words, does this phenomenon have specificity toward the material of confined surfaces?

doi:10.6342/NTU202404416

This is another question that we wanted to solve.

1.5 Highlight of this work

In this thesis, we utilize the SFA as the main technique, combined with the video analysis method to answer the following question concerning the confinement-induced HER.

1. Why does the confinement induce the HER to happen at lower overpotential?
2. Is the event triggered only by confinement itself, or the surface properties of mica is also important?
3. How does the event conquer the mass transport problem?

doi:10.6342/NTU202404416

Chapter 2 Experimental Section

2.1 Materials and Chemicals

1. Au target: 99.9%, purchased from LEESAN PRECIOUS METAL CO., LTD.
2. Ag target: 99.9%, purchased from LEESAN PRECIOUS METAL CO., LTD.
3. Muscovite mica: it was obtained from S & J Trading Company (NJ, USA) as roughly 15 × 15 cm ruby-colored sheets with 2–3 millimeters thickness, and the grading for it is V1 grade.
4. Sulfuric acid (H_2SO_4): 95%, purchased from FLUKA CHEMICALS LIMITED
5. Optical glue: which will be curbed under UV light, is purchased from Norland Adhesive, number 81, UNICE E-O SERVICES INC.
6. quartz cylindrical disc: purchased from CONTROL OPTICS TAIWAN INC., the radius for the disc is 1 cm.
7. Milli-Q water: the resistance is larger than 18 M ohms, which is used to prepare the 0.5M sulfuric acid (pH = 0.1 to 0.2) from 95% sulfuric acid.
8. Argon for sputtering: purchased from FONG-MING GASES INDUSTRIAL CO., LTD.

doi:10.6342/NTU202404416

2.2 Surface force apparatus

The Surface Force Apparatus (SFA) is an instrument that measures the inter-molecular force acting between two cross-cylindrically arranged surfaces as well as measures their separation distance.

SFA uses two curved and molecular smooth surfaces opposite to each other; one is the back-silvered mica surface, and the other is the gold surface. The semi-transparent silver and gold layer forms an interferometric cavity that, when light passes through, creates an interference pattern within the confinement area. The pattern is wavelength, and hence, separation distance dependent, which can be used to get the separation distance of the two surfaces (shown in subsection 2.2.2). The direction of two surfaces is set in cross-cylinder form to measure the interaction force between the two surfaces. According to the Derjaguin approximation, the cross-cylinder orientations can be approximated to sphere versus sphere or sphere on the flat model, which helps us to investigate the interaction force between two surfaces that are only contacted at one specific point.

2.2.1 Structure of SFA

The home-built SFA set-up (Figure 2.1[30]) has been described in more detail elsewhere[30] but in short, in Figure 2.1[30]-a), we can see that the SFA setup consists of multiple different components. The first one is the fluid cell, which is magnified in Figure 2.1[30]-b). It is equipped with a three-electrode system for electrochemical measurements: the mounted surfaces act as the working electrode (WE), connected with a short gold wire pressed onto the surface to connect to the potentiostat. The WE is surrounded by

doi:10.6342/NTU202404416

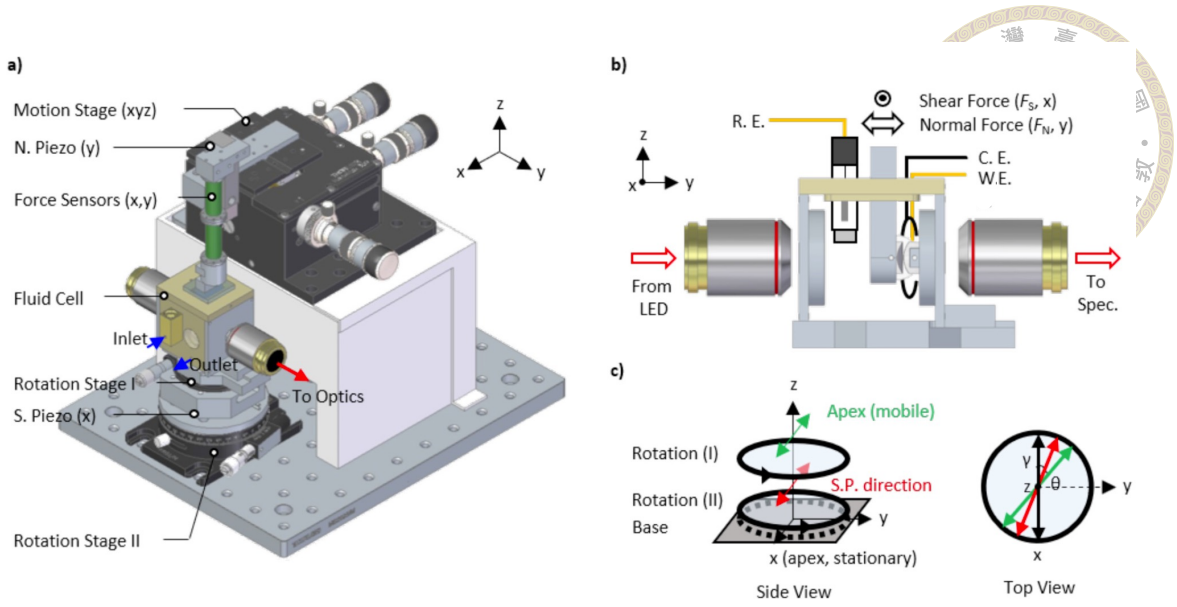

Figure 2.1: (sSFA)Operation principle of angle-corrected in situ sensing surface forces apparatus (SFA). (a) Overview of the home-designed sSFA and (b) cell geometry. (c) Angle correction for a shear experiment involving two rotation mechanisms to compensate for the misaligned angle of γ and θ between the shear promotion direction to the two surface apex directions, respectively.

the counter electrode (CE), which is a platinum wire. The reference electrode is a silver-silver chloride mini electrode in a saturated potassium chloride solution. The potential difference between our reference electrode and Reversible Hydrogen Electrode (R.H.E.) is 0.1976 [V], so we can also use the formula in Equation 2.1to transfer the potential vs. Ag/AgCl to vs. R.H.E.

$$E_{\mathrm{RHE}} = E_{\mathrm{Ag/AgCl}} + 0.0592 \times \mathrm{pH} + E_{\mathrm{Ag/AgCl,\ standard}} \tag{2.1}$$

where,

- E_{RHE} is the potential relative to the Reversible Hydrogen Electrode (RHE)
- $E_{\mathrm{Ag/AgCl}}$ is the measured potential relative to the Ag/AgCl reference electrode
- pH is the pH value of the electrolyte. In our experiment, it is usually 0.16, which is the measured value by the pH meter before the experiment starts.

doi:10.6342/NTU202404416

- $E_{Ag/AgCl,\ standard}$ is the standard potential of the Ag/AgCl electrode relative to SHE (0.1976 V at 25°C)

As for the optical system, the light from the LED light source will penetrate the electrochemical cell and be split by the beam splitter.

In the SFA setup, we use two sets of light detectors. One is the Charge-Coupled Device (CCD) camera, which can give the *in-situ* image of the surface and help the performer check whether there's a contaminant on the surface. Besides, it can also help us to quickly find the focal plane of the optical system. Another is the spectrometer, which helps us to analyze the distance between two surfaces by the Fringes of Equal Chromatic Order (FECO). (detailed will be discussed in the subsection 2.2.2). This part of the light will first be cut by the narrow slit and finally arrive at the spectrometer to get the FECO pattern. When the separation distance varies, the FECO pattern will also show a wavelength shift, which can then be analyzed as the distance change by the Multiple Beam Interferometry (MBI).

In order to perform force vs. distance measurements and create well-defined confinement conditions, the surfaces are able to approach and separate via a set of XYZ micro meter translation stages as well as a y-direction piezo actuator for nanometer precision movement. The surface platform is also connected to a commercial force sensor to sense the acting intermolecular forces between surfaces during approach and separation. The force sensor measures force with a semi-conductor strain gauge, providing high accuracy and sensitivity force data.[30, 31]

The ideal model for measuring the force and distance between the surfaces is the sphere-on-flat model. However, the preparation of mica surfaces (details are discussed

doi:10.6342/NTU202404416

in subsection 2.3.3) needs to make mica pieces attached to a sphere substrate, which is hard to achieve. Consequently, we make the mica pieces attached to the cylinder disc, which makes surface preparation easier. As a result, the SFA setup makes the two surfaces mounted in a 90-degree crossed phase, which is mathematically regarded as equal to a sphere-on-flat geometry[32].

2.2.2 Multiple beam interferometry

SFA uses Multiple Beam Interferometry (MBI) to measure the distances between two surfaces during the experiment. MBI was first introduced by Tolansky *et. al.*. The principle of MBI is that when a broad band of light is transmitted through two semi-transparent surfaces in close proximity, it will form standing waves between two surfaces when the wavelength of the light meets the constructive interference boundary condition. This will manifest in the camera image as a light-dark alternative pattern, which is called Newton Ring (NR). Once the image passes through a spectrometer slit that cuts the NR, we get the Fringes of Equal Chromatic Order (FECO). The picture of NR and FECO pattern is displayed in the Figure 2.2. (a) is the NR, which can give us information on whether the *in-situ* video is in focus and tell us the location of the contact point in the detected area. (b) is the FECO pattern, the flattered pattern is the region where two surfaces are contacted and deformed to form a flat region. D_r means the radius of contact of the deformed surfaces.

Before the mathematical derivation, we first need to construct a geometry model that helps us to discuss the formula and parameters. The model of MBI is illustrated in Figure 2.3, which assumes that there is one liquid layer that is sandwiched by two mica layers, and the outer part of the mica layer is coated with silver. The electromagnetic wave of the injection light is set to be Equation 2.2.

doi:10.6342/NTU202404416

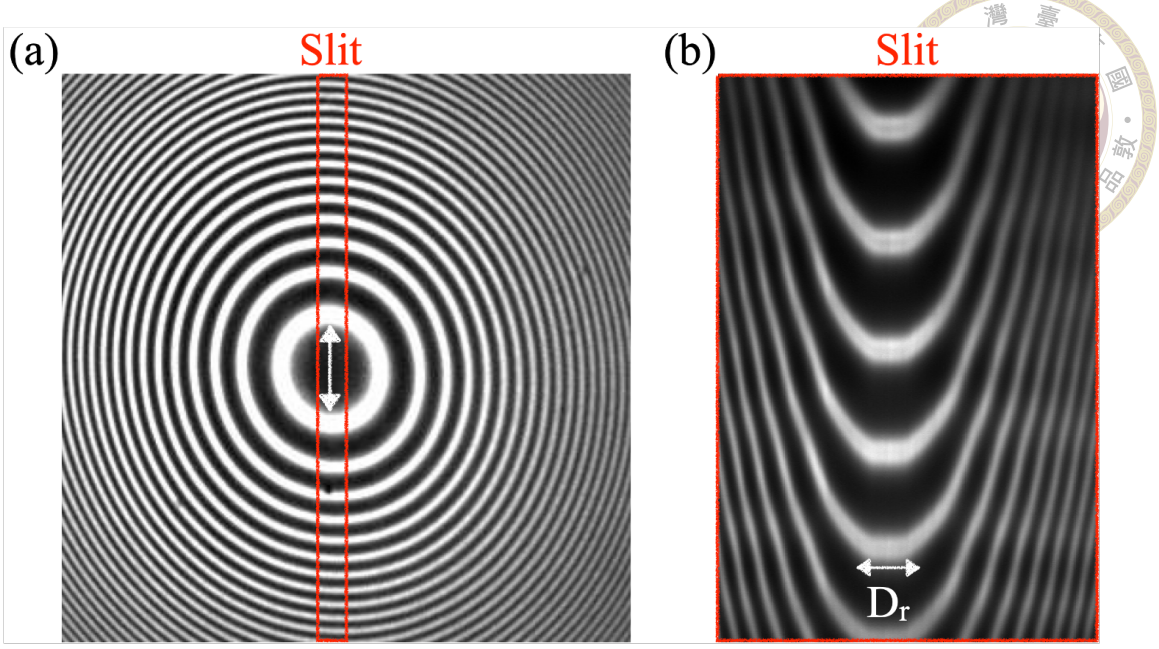

Figure 2.2: The information got from SFA setup (a) The NR (b) The FECO pattern got by cutting the NR by a narrow slit

$$E(x) = A_m e^{i(kx)} \tag{2.2}$$

where A_m is the amplitude of the electromagnetic wave, i is the imaginary number, k is the wavenumber of an electromagnetic wave and equals to $\frac{2\pi}{\lambda}$, λ is the wavelength of the light.

The light is first directed onto the left-hand side in Figure 2.3, then penetrates the sandwiched system, constructing multiple reflections, and finally goes through the system to the detector. The refractive indexes for both layers are denoted as n_{mica} and n_{liquid}. The thickness of the mica layer and liquid layer is set to be Y and T, respectively. The objective of the MBI is to calculate the mathematical relation of liquid thickness T with other parameters, and it will be discussed later. The geometry system here is modified from the reference [33].

According to the reference [33], the general solution for a three-layer system (two

doi:10.6342/NTU202404416

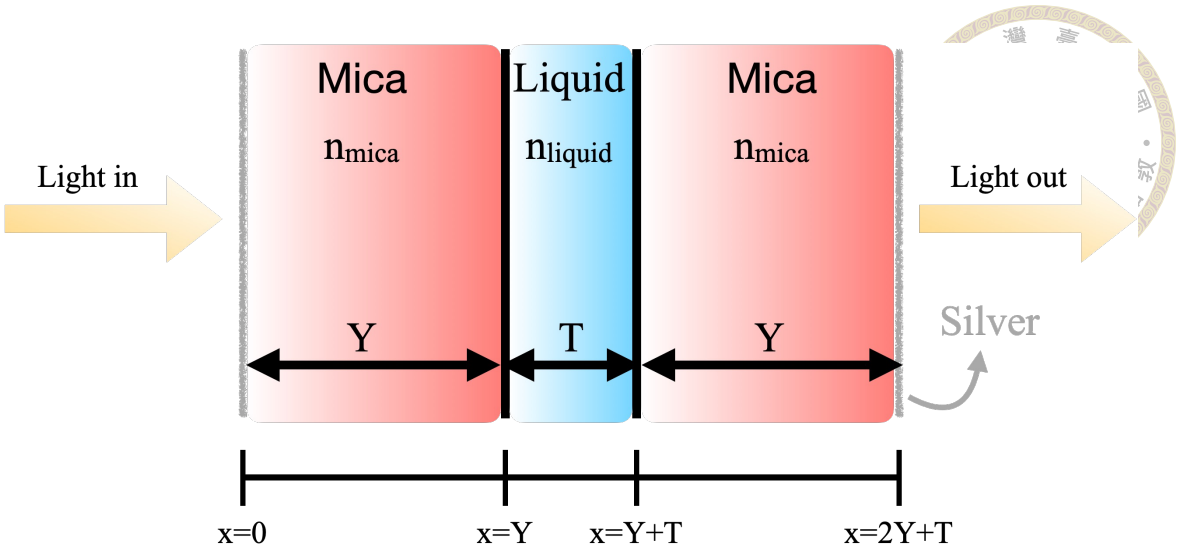

Figure 2.3: The schematic diagram for multiple beam interferometry derivation

back-silvered mica surfaces sandwiching a liquid layer) can be obtained. This solution reveals the relationship between the liquid layer thickness, the refractive indices of mica and liquid, and the wavenumber of the electromagnetic wave, as shown in Equation 2.3.

$$\tan(kn_{liquid}T) = \frac{(1-r^2)\sin(2kn_{mica}Y)}{2r-(1+r^2)\cos(2kn_{mica}Y)} \qquad r = \frac{n_{mica}-n_{liquid}}{n_{mica}+n_{liquid}} \tag{2.3}$$

When the two mirrors are in contact, theoretically, there will be a liquid layer of zero thickness between the two mirrors, so the thickness of the liquid layer (T) equals zero. As a result, the left-hand side of Equation 2.3 would be zero, which causes the sine function on the right-hand side should also become zero. Thus, we can get the relation that,

$$2kn_{mica}Y = n\pi \qquad n = 1, 2, 3, \ldots \tag{2.4}$$

where n is the order of interference, which is a natural number.

The Equation 2.4 can be further simplified to

doi:10.6342/NTU202404416

$$2n_{mica}Y = \frac{n\pi}{k^0} = \frac{n\lambda^0}{2} \tag{2.5}$$

where k_0 and λ^0 are the wave number and wavelength of the electromagnetic wave that passes through the system when it is contacted.

When the liquid thickness changes, the wavelength will start to redshift from λ^0 to λ. Then we can get the relationship that

$$2kn_{mica}Y = (2n_{mica}Y)(k) = \frac{n\lambda^0}{2}\frac{2\pi}{\lambda} = n\pi(1 - \frac{\lambda - \lambda^0}{\lambda}) = n\pi(1 - \frac{\Delta\lambda_n}{\lambda}) \tag{2.6}$$

If we replace the relationship got in Equation 2.6 to Equation 2.3, we can get the following equation:

$$\tan(kn_{liquid}T) = \frac{2\bar{\mu}\sin(n\pi\Delta\lambda_n/\lambda)}{(1+\bar{\mu}^2)\cos(n\pi\Delta\lambda_n/\lambda) \pm (\bar{\mu}^2 - 1)} \tag{2.7}$$

$$\bar{\mu} = \frac{n_{mica}}{n_{liquid}} \tag{2.8}$$

The $\pm$ is decided by the even and odd numbers of n. When the n is odd, the sign of it would be positive, and vice versa. Suppose the thickness of the liquid layer is small (nanometer scale). In that case, the triangular function can be further simplified, and we can tidy up those symbols and get the general solution for liquid thickness and wavelength shift.

$$\begin{aligned} T &= \frac{n\Delta\lambda_n}{2n_{mica}} && \text{for } n \text{ is odd} \\ Tn_{liquid}^2 &= \frac{nn_{mica}\Delta\lambda_n}{2} && \text{for } n \text{ is even} \end{aligned} \tag{2.9}$$

doi:10.6342/NTU202404416

Using Equation 2.9, we can proceed fitting process from FECO data and get the liquid thickness data. Note that the mathematics above discusses liquid thickness between two back-silver mica surfaces. Our experiment is analyzing the liquid thickness between back-silver mica and gold mirrors, so the math will differ slightly. We used the SFA explore software to do the liquid thickness analyzing procedure, which is developed by Schwenzfeier et al. [34] using the transfer matrix method to fit the FECO data; the detailed mathematics derivation is shown in previous works [34].

2.3 Surface preparation

2.3.1 Magnetron sputtering

In order to form the interferometric cavity as well as the electrode surface, we need to prepare atomically flat metal thin films. Magnetron sputtering (MS) is a physical vapor deposition (PVD) technique suitable for preparing clean, flat metal surfaces [35].

The procedure of MS to conduct PVD can be separated into four parts: gas ionization, ion bombardment, magnetic field-assisted enhancement, and atom deposition.

The procedure of gas ionization are as follows:

1. Pumping down the sputtering chamber to operational vacuum level, usually in the magnitude of $\sim 10^{-3}$ to 10^{-2} mbar.[36]. The vacuum environment removes traces of contaminants in the air and reduces background pressure that interferes with the deposition.

2. Introducing some gas molecules into the vacuum chamber; In order to prevent the

doi:10.6342/NTU202404416

gas molecules from reacting with the target material, we usually use argon (Ar) as the inlet gas. Another advantage of using Ar is its easy ionizability.[37]

3. High voltage, ranging from hundreds or thousands of volts, is applied on the target (cathode) and substrate (anode). The high voltage causes the argon gas to become ionized, forming a plasma. A large amount of Ar^+ and electrons will be produced in this period.

In the ion bombardment process, the electric field would force the argon ions(positive charged) to speed up and bump into the target (negative electrode), causing atoms or molecules of the target material to be ejected from the surface[36]. This process is similar to a series of tiny impacts and peeling actions. The accelerated Ar^+ have high kinetic energy; they will pass the energy to the target atoms, which are impacted by it, giving them enough kinetic energy to travel in the chamber.

A magnet will be behind the target, and the magnetic field direction will be perpendicular to the electric field direction. This magnet will force the electrons produced at the gas ionization stage to spiral along the magnetic field line, increasing the residence time for electrons near the target. This kind of motion is referred to as ”magnetron electron motion.” Owing to the increment of the number of electrons near the target by magnetron electron motion, the possibility of electrons colliding with argon gas will increase, causing more argon gas to be ionized. These phenomena increase the density and stability of the plasma, enhancing the efficiency of the MS.

The atoms that escape from the target material will start to travel in the chamber; since the vacuum level of the chamber stays low pressure, the atoms can usually fly linearly without scattering. After long travel, the atoms will be located on the substrate and form a

doi:10.6342/NTU202404416

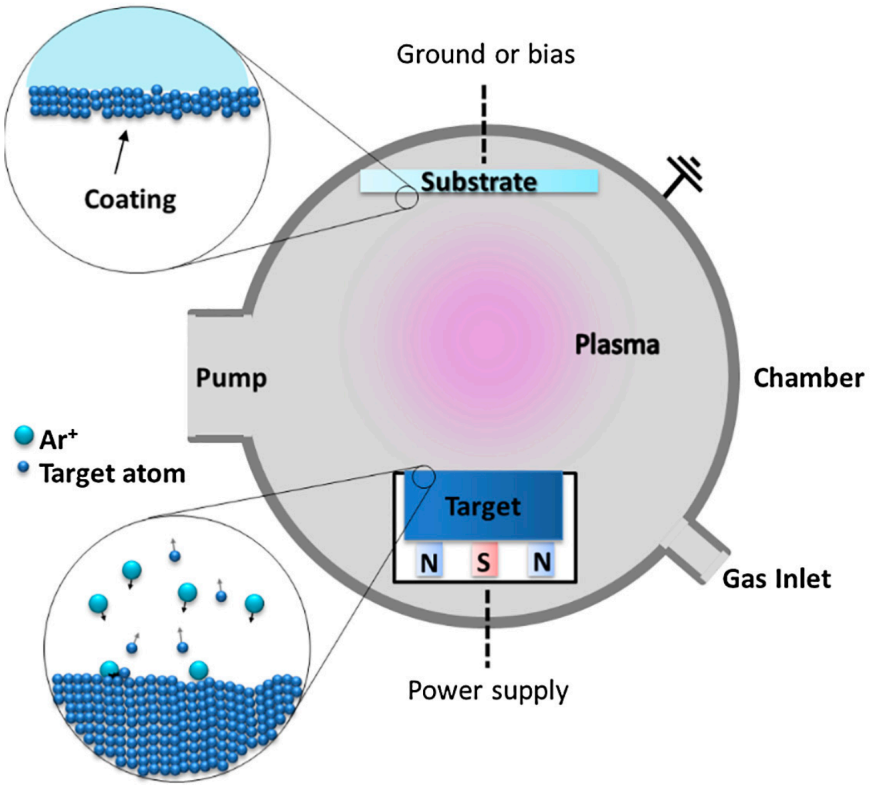

Figure 2.4: Magnetron sputtering schematic diagram

thin film. They will diffuse and transport on the substrate until they don't possess enough kinetic energy and are located in one specific position on the substrate.

Figure 2.4[38] is the schematic figure that illustrates the working principle of MS as discussed above.

The sputter condition parameter in our experiment is shown in Table 2.1.

Target	Sputter Time	Sputter Current	Ar Pressure	Estimated Thickness
Au	270 sec	50 mA	1.1 x 10^{-3} torr	40 nm
Ag	105 sec	80 mA	1.1 x 10^{-3} torr	40 nm

Table 2.1: Sputtering parameters used in our experiment

doi:10.6342/NTU202404416

2.3.2 Template stripping method

The gold layer on the quartz disk is prepared using the template stripping method (TSM). We use Muscovite mica as the template for the gold layer to sputter on. The reason for choosing Muscovite mica is that it is easier to prepare a uniform and atomically flat surface.[33, 34]

We first slice the commercial Muscovite mica into thin pieces and control the thickness to be a bendable sheet in order to make it totally attached to the glass convex in the following procedure. After we slice the mica sheet into thin pieces, we apply the TSM procedure to produce our gold surface and the procedure of TSM is as follows, and the schematic diagram for TSM procedure is shown in Figure 2.5:

1. Sputtered the gold particles on the top of the mica surface through MS.

2. Dropped the optical glue on top of the quartz disc and attached the just-sputtered gold surface to the glue layer.

3. Put weight on the edge of the disc to make the mica bent to fit the curvature of the disc; since the quartz disc surface is curved (radius is 1 centimeter), when we put a plane gold surface on top of it, it can not fully attach the whole disc surface.

4. Put the samples under a UV light overnight to cure the epoxy glue, and the gold surface will firmly stuck to the disc by optical glue.

5. Stripped off the mica surface and getting the atomic level flat gold surface on the quartz disc

doi:10.6342/NTU202404416

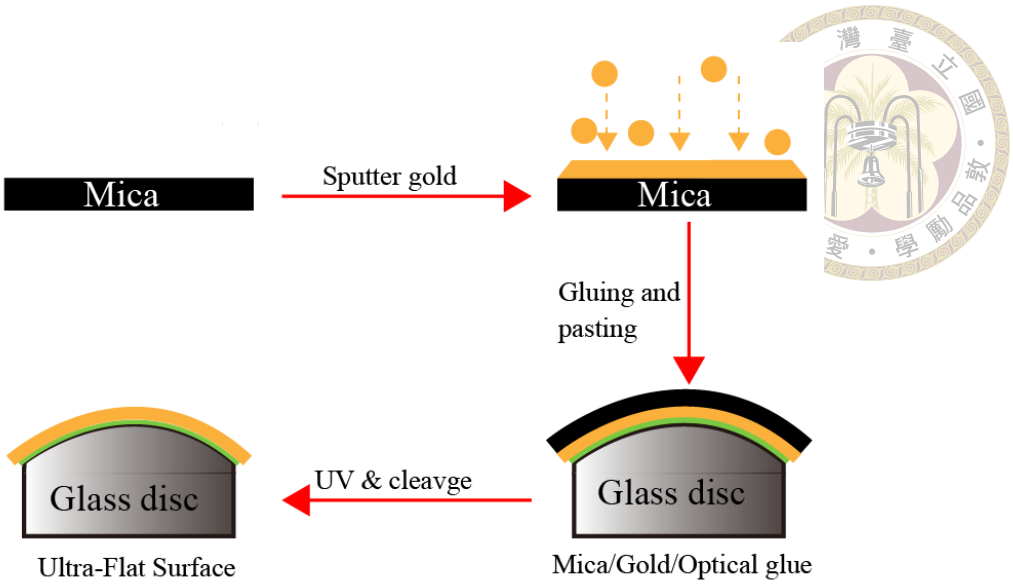

Figure 2.5: The procedure of template stripping method

2.3.3 Preparation of back-silvered Mica surface

In the SFA setup, we use the back-silvered mica surface to contact with the gold surface (WE). First, we cleave a thin piece of mica sheet (3-6 μm). Second, the mica piece will be sputtered to deposit a silver layer on the mica surface. Then, we used optical glue to make the silver surface adsorbed on the glass convex, which exposed the mica surface at the top, and the silver surface was sandwiched in the middle to be a silver mirror to construct an interference pattern.

2.3.4 Structure of Muscovite mica

Muscovite mica is an alumino-silicate mineral[39], whose chemical formula is ($KAl_2(Si_3Al)O_{10}(OH)_2$[40]). Muscovite mica exhibits a unique layered structure, which is depicted in Figure 2.6[40]. We can find that the potassium ions are sandwiched in between the layer structure. After we slice the Muscovite mica, which is described in our sample preparation method, actually we expose the potassium on top of the surface. However,

doi:10.6342/NTU202404416

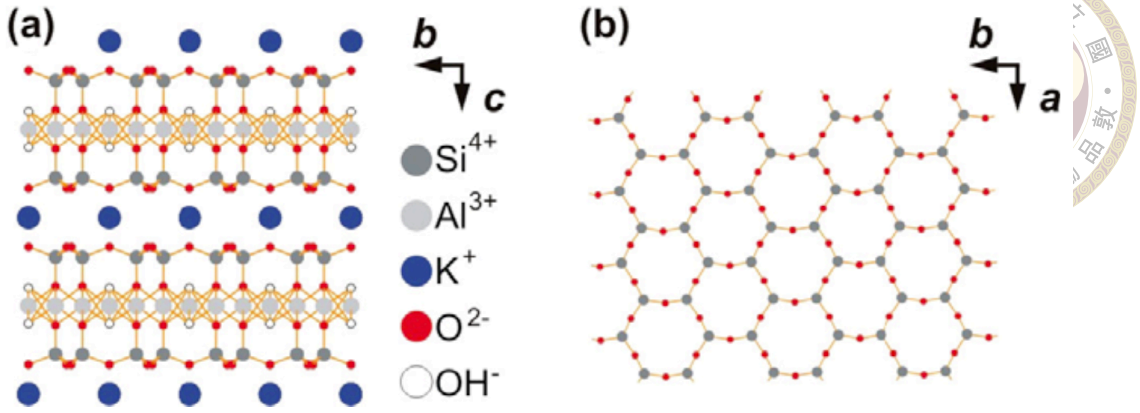

Figure 2.6: Diagram illustrating the crystal structure of Muscovite mica. Vectors a and b define the 001 planes, with vector c representing the surface normal vector. (a) Side view (projection onto the a-axis) showing layers of alumino-silicates separated by interlayer potassium ions held together by electrostatic forces.(b) The hexagonal pattern of the top 001 surface layer (projection onto the c-axis), displaying silicon (partly aluminum) and oxygen atoms of a cleaved mica surface, excluding residual potassium ions.

if the mica surface is put into an aqueous solution, the potassium exposed on the surface would dissociate into water, making the surface of mica bear a high charge density, which is roughly -0.1 to -0.3 Coulomb per meter square.[41, 42]

2.4 Electrochemistry

In this study, we applied several electrochemical analysis techniques. In this section, we briefly introduce their working principle, parameters, and the reason why we chose to use these techniques.

2.4.1 Linear sweep voltametry

Linear Sweep Voltametry is a powerful technique for analyzing the kinetics of the electrode. The procedure of the LSV technique uses a constant scan rate (unit: V/s) and scans from the given initial potential to the ending potential. While scanning, the potentiostat will record the amount of current response on the working electrode, which arises

doi:10.6342/NTU202404416

from the redox reaction at the surface. Usually, the current would gradually increase if the applied potential increases until the redox species are consumed on the electrode and the current decreases again. The applied potential and current response can be plotted as a voltammogram.

The parameters in our experiment for LSV are shown in Table 2.2.

Parameter	**Value**
Potential Sweep Range	0 V to -0.7 V vs. sat. Ag/AgCl reference electrode
Scan Rate	-10 mV per second
Interval of Data Acquisition	10 mV/s

Table 2.2: Experimental parameters for LSV

2.4.2 Chronoamperometry

Chronoamperometry is the application of a constant potential on the working electrode. At the beginning of applying potential, a charging current will appear, which arises from the potential difference between the applied potential and the open circuit potential (OCP) of the electrode surface. This potential difference causes the surface to start to accumulate charge, hence the term ”charging current.”

The current, when applying the potential, should follow the Cottrell equation.

$$i = \frac{nFAc_i^o\sqrt{D_i}}{\sqrt{\pi t}} \tag{2.10}$$

where i is the current (A), n is the number of electrons transferred in the redox reaction, F is the Faraday constant (96485 C mol^{-1}), A is the area of the working electrode (cm^2), and c_i^o is the initial concentration of the redox species (mol/cm^3). D_i is the diffusion coefficient of the species (cm^2/s), and t is time (s).

doi:10.6342/NTU202404416

The purpose of using a chronoamperometry (CA) technique is to apply a constant overpotential for an extended period to observe the redox current change over time, allowing us to obtain information about the stability of the catalyst.

2.4.3 Open Circuit Potential

The open circuit potential (OCP) is the potential difference between the electrolyte and the electrode when no current passes through the electrode. Specifically, it can be defined as the potential difference between the working electrode and the reference electrode (RE) when no current exists. According to the definition, the OCP can be expressed as Equation 2.11.

$$E_{\mathrm{OCP}} = E_{\mathrm{WE}} - E_{\mathrm{RE}} \tag{2.11}$$

The value of OCP can tell us plenty of useful information. Firstly, the OCP is the equilibrium potential for all the electrochemistry reactions mixed together[43]; at this potential, the oxidization and reduction rates are the same for all responses. Secondly, the OCP value can give us information on material stability. If the OCP is too close to the corrosion potential of the electrode material, the material will show high instability in this kind of electrolyte environment. Finally, the OCP can reveal information about the general state of the electrode such as ion adsorption/ desorption on the electrode or the formation of an oxide layer on the electroe surface.[44]

doi:10.6342/NTU202404416

2.5 Comsol Multi-Physics modeling

Comsol Multi-Physics is a commercial software that can model various physics configurations. It uses the finite element method to solve the partial derivative equation on a mesh grid. In electrochemistry, we are usually concerned about charge conservation and current conservation problems coupled together, and this can be modeled by solving the related partial differential equations. (PDEs)[45]

According to the literature[46], the electrode potential will be increased by confinement, which may give the confinement-induced HER a reasonable explanation. Since we can't get the surface potential from the SFA due to the high ionic strength of our electrolyte, we decided to use Comsol Multi-Physics to model the surface potential distribution on the working electrode.

In the application, we choose secondary current distribution coupled with the dilute species transportation models to calculate the potential distribution.

2.5.1 Secondary current distribution

The secondary current distribution assumes that the concentration of ions is homogeneous and doesn't vary with the electrolyte's location, making it easy to solve the PDEs without mass transfer. (But mass transfer is important in many cases; we'll use another physics field called dilute species transportation to reconsider mass transport.) In addition, it also hypothesizes that the conductivity of the electrolyte is constant; this makes it easy to use the simple Laplace function to solve the potential distribution. Equation 2.12 is the so-called Laplace equation, where ψ is the electric potential, and the Laplace equation

doi:10.6342/NTU202404416

describes the potential distribution in the electrolyte.

$$\nabla^2 \psi = 0 \tag{2.12}$$

Another PDE that needs to be solved is the current conservation equation, shown in Equation 2.13, where J is the current density and σ is the conductivity of the electrolyte.

$$\nabla \cdot J = 0, \quad J = -\sigma \nabla \psi \tag{2.13}$$

The final PDE is the electrode kinetics of the reaction. Usually, we use the Bulter-Volmer equation[47] to describe the electrode kinetics. Equation 2.14 is the Bulter-Volmer equation, where J_0 means exchange current density; α_a and α_c are the charge transfer coefficient for anodic and cathodic reaction, respectively.

$$J = J_0 \left(e^{\frac{\alpha_a F \eta}{RT}} - e^{-\frac{\alpha_c F \eta}{RT}} \right) \tag{2.14}$$

In this model, we first assume the separation of charges at the interface when high potentials are applied to the surface and the bulk is not so obvious since the concentration of electrolyte is high enough to quench out the surface potential efficiently close to the electrode. Then, we assume the reactions on the electrode surface are very fast, which means the reaction is kinetic control, to simplify the calculation. By considering these two assumptions, we think it is safe to apply the Bulter-Volmer equation to the electrode kinetic.

doi:10.6342/NTU202404416

2.5.2 Dilute species transportation

Since the secondary current distribution physics field neglects the mass transport in the system, we need to introduce another physics field to account for it: the dilute species transportation physics field. The dilute species transportation model considers the Nernst-Plank equation to describe the motion of ions in the electrolyte during the electrochemical process through migration and diffusion.

The Nernst-Planck equation (shown in Equation 2.15) describes the mass transportation flux of ions due to diffusion, migration, and convection in the system.

$$\mathbf{J}_i = -D_i \nabla c_i - z_i u_i c_i \nabla \phi + \mathbf{v} c_i \tag{2.15}$$

In this equation, $\mathbf{J}_i$ represents the mass transport flux of species i, which indicates the transportation rate at which species i move through a unit area per unit time. The term D_i denotes the diffusion coefficient of species i, reflecting how quickly i diffuses in the medium. The variable c_i stands for the concentration of species i, representing the number of i per unit volume. The charge of i is indicated by z_i, which specifies the number of elementary charges carried by each ion of species i. The mobility of i is represented by u_i, describing the velocity of i per unit electric field, and $\mathbf{v}$ represents the velocity of the bulk fluid.

The first term of Equation 2.15 is regarding the diffusion effect, while the second term describes the migration effect. The last term is regarding convection in the system; however, since the SFA setup uses stationary electrolyte conditions, we neglect the influence of convection. (but the bubble-induced micro convection will be also neglected,

doi:10.6342/NTU202404416

and that's is the limitation of this model) Another PDE that needs to be considered is the Poisson equation (Equation 2.16, which describes the charge density distribution for the ions in the electrolyte.

$$\nabla^2\phi = -\frac{\rho}{\epsilon} \tag{2.16}$$

where ρ is the charge density, which describes the charge distribution in the space; ϵ is the relative permittivity of the electrolyte, which describes how well an electrolyte shields the potential in the space. If the value of relative permittivity is high, the electrolyte can reduce the electrolyte field in the space, which lowers the mobility of ions through migration.

2.5.3 Model Geometry

The geometry we use to simulate the two curved surfaces that serve as the gold surface and mica surface are arranged opposite to each other, while one counter electrode circulates the gold surface. We use a box to enclose the surfaces and serve as the electrochemical cell. The cell space is filled with sulfuric acid. The actual shape of the geometry model can be seen in Figure 2.7.

2.5.4 Boundary conditions in our experiment

The boundary conditions, which are critical factors in this simulation, are as follows.

1. The applied potential on the working electrode is -0.6 V
2. The potential on the counter electrode is 1.5 V, which is based on experimental data from the potentiostat when applying -0.6 V on the working electrode.

doi:10.6342/NTU202404416

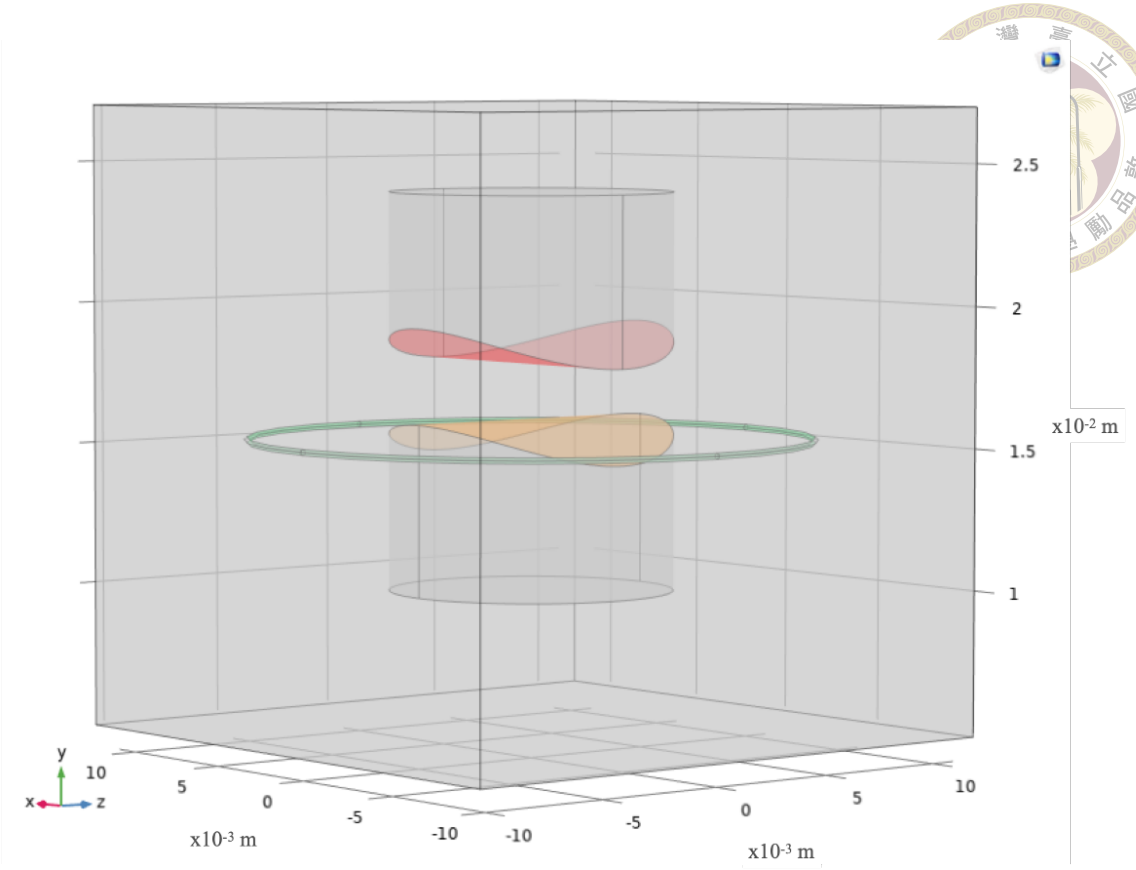

Figure 2.7: 3D Geometry in Comsol-Multiphysics, the orange surface is gold surface, which is surrounded by the counter electrode (green circle); the red surface is used to model the Muscovite mica surface

3. The electrolyte conductivity of 0.5M H_2SO_4 is 23.6 S/m.[48]

4. The mica surface is set to be an insulated surface.

5. The separation distance between the gold surface and mica surface is set at 0 μm, 10 μm, 100 μm, and 2 mm, respectively

6. The electrode kinetic for both WE and CE is set to obey the Butler-Volmer equation.

doi:10.6342/NTU202404416

2.6 Calculating and modeling proton concentration near electrode surface

2.6.1 Modeling the proton concentration profile

The simulation from Comsol is mainly used to model the surface potential distribution that we desire to know. However, the limitations and assumptions of Comsol make it hard to get the proton concentration profile near the working electrode similar to the real world. As a result, we try to use some PDEs to solve the proton concentration in a simple 1-dimensional model by Python script, the electrochemistry concept of the calculation is written below.

The Poison-Boltzmann equation can give us information on potential and ion distribution in the electrolyte, which is shown in Equation 2.17, where z is the charge of ions, e is the charge of electrons, ρ_0 is the charge density of the bulk solution, which can be calculated through equation Equation 2.22, $\psi(x)$ is the electric potential at position x, k_B is the Boltzmann constant. This section only considers the Poisson-Boltzmann equation in a 1-dimensional space to simplify the problem.

$$\frac{d^2\psi}{dx^2} = -\frac{Ze\rho_0}{\epsilon}\exp(-\frac{Z_i e\psi(x)}{k_B T}) \tag{2.17}$$

The analytical, non-linear solution for the Poisson-Boltzmann equation, called the Gouy-Chapman solution, can give us a more exact value of the potential distribution close to the experimental case. The Gouy-Chapman solution is shown in Equation 2.18, where ψ_s stands for surface potential, which can be calculated with the Grahame equation (shown

doi:10.6342/NTU202404416

in Equation 2.20, κ is the reciprocal of the Debye length (λ_D) and the formula for λ_D is shown in Equation 2.19, where I is the ionic strength.

$$\frac{\tanh\left(\frac{\psi(x)}{4}\right)}{\tanh\left(\frac{\psi_s}{4}\right)} = \exp(-\kappa x) \tag{2.18}$$

$$\lambda_D = \frac{1}{\kappa} = \sqrt{\frac{\epsilon k_B T}{\sum_i Z^2 e^2 \rho_0}} = \frac{0.304}{\sqrt{I}} \tag{2.19}$$

To get the value of surface potential as a boundary condition to do simple modeling, we introduced the Grahame equation to calculate the surface potential under specific concentrations of electrolytes. The Grahame equation is shown in Equation 2.20, where σ_s denotes the surface charge, and the surface charge of mica is set to be -0.2 C/m^2, and n_0 is the number density of the electrolyte, meaning the number of ions per m^2, and ϵ stands for the permittivity of the electrolyte.

$$\sigma_s = \sqrt{8\epsilon k_B T n_0}\sinh\left(\frac{ze\psi_0}{2k_B T}\right) \tag{2.20}$$

We used the analytical solution of the Poisson-Boltzmann equation to calculate the potential distribution of the mica surface and the gold surface. The surface potential of mica can be calculated from the surface charge of mica, while the surface potential of gold is set to be 0 v and -0.1 V to model the equilibrium state and apply certain potentials on the gold electrode state. Then, we sum the potential distribution of the two surfaces and get the total potential distribution in the space.

After that, we use the Boltzmann distribution shown in Equation 2.21 to convert the potential distribution to the charge density distribution.

doi:10.6342/NTU202404416

$$n_x = n_0 \exp\left(\frac{e\psi}{kT}\right) \tag{2.21}$$

Note that because the potential we got from mica and electrode is negative potential, the charge density will also calculate a negative ions distribution. We assumed that the proton in the electrolyte will compensate for the negative charge distribution by the same amount of positive charge density, so we can convert the positive charge density to proton concentration by the formula shown in Equation 2.22 simply through give the total potential distribution a negative sign. Equation 2.22 is very helpful in calculating the bulk charge density from bulk concentration and correspondent concentration at poison x from charge density at position x.

$$\rho_x = C_i \times 1000 \times N_A \times e \tag{2.22}$$

where N_A is the Avogadro's number. By applying Equation 2.22, we can finally get the proton concentration profile in the confined region.

In short, we use the Grahame equation to solve the surface potential and derive this value into the analytical solution of the Poisson-Boltzmann equation to get the potential distribution in the electrolyte. Then, the potential distribution in the space is calculated by adding the potential distribution of mica and gold surface. After that, the Boltzmann distribution was used to get the charge density distribution. Finally, the charge density distribution is converted to concentration distribution. The mathematical calculations were performed using a Python script. Since we are not well-versed in coding, we utilized ChatGPT to assist with the coding process. We provided the requirements and the chosen formulas, and ChatGPT helped convert our ideas into Python code. The script is included

doi:10.6342/NTU202404416

in Appendix A.

The boundary condition for the proton concentration profile modeling is as follows:

- Temperature (T_{emp}): 298.15 K
- Surface charge density of mica (σ_s): -0.2 C/m^2
- Permittivity of the electrolyte (ϵ): 7.083×10^{-10} F/m
- Electrolyte concentration at both surfaces: 0.5 M
- Debye-Hückel parameter for both mica and gold surface (κ): 2.33 nm^{-1}
- Surface potential of gold surface: 0 V and -0.1 V
- Distance Between Surfaces (d): 1, 2, 3, 4, and 5 nm

2.7 Bubble size calculation

As is discussed in subsection 1.3.2, the bubble size may play an important role in the overpotential that we measured. Hence, it is crucial to calculate and statistic the bubble size of hydrogen during the catalytic process. Fortunately, the SFA setup provides us with a clear top view of *in-situ* videos of the electrode surface, which enables us to do further image processing to analyze the bubble cross-section area under different separation distances when the hydrogen is evolving.

We use a Python script to analyze the *in-situ* video of bubble formation to calculate the bubble cross-section area (the script is shown in Appendix B). The procedure is as follows.

doi:10.6342/NTU202404416

1. Slicing the *in-situ* video into many individual frames (the script will not be shown in Appendix B).

2. Applying a background subtraction to remove the dirt or contaminants on the camera or gold surface. The procedure is as follows:

    - Transfer each frame as a matrix of brightness at every pixel.
    - Use all matrices of every frame to subtract the matrix of the first frame.
    - This process yields the relative intensity change compared with the first frame, removing the influence of the background.
    - Re-plot the frames in a gray-scale filter using the relative intensity matrices of each frame.

3. Depicting the contour of bubbles in two steps:

    - We observed that bubbles in micro- or nano-confined situations deform into a thin bubble layer. The border of the layer scatters light, while the inner part remains unaffected and shows similar intensity to regions without bubble formation.
    - To utilize this observation, we calculate the intensity gradient of every pixel and connect the high gradient pixels to form a closed contour, regarded as the bubble cross-section shape.

4. Calculating the area of each contour:

    - The script treats the contour as a polygon containing many vertices, denoted as (X_0, y_0), (X_1, y_1), (X_2, y_2), …, (X_{n-1}, y_{n-1}), where (X_n, y_n) equals (X_0, y_0), creating closed contour vertices.

doi:10.6342/NTU202404416

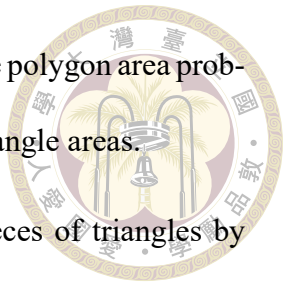

- We apply the Shoelace formula (Equation 2.23) to solve the polygon area problem, an extension of the Gauss formula for calculating triangle areas.
- The Shoelace formula slices the polygons into many pieces of triangles by fixing one point to be the vertex of all triangles (usually is (X_o, y_o)) and taking the nearby point as another two vertices, e.g. (X_1, y_1), (X_2, y_2); (X_2, y_2), (X_3, y_3), in this way, we sliced the contour into pieces of non-overlapping triangles. Then, all triangle areas will be added to the sum area.

$$Area = \frac{1}{2}\left|\sum_{i=0}^{n-1}(x_i y_{i+1} - x_{i+1} y_i)\right| \tag{2.23}$$

After conducting the procedure above to decide the bubble cross-section area. Surprisingly, we found many outliers that will affect the result, such as the dart on the camera, the contamination near the surfaces, and so on. In order to decrease the impact of outliers that affected the experiment, we started to add some restrictions on the depicted contours to remove the outliers.

1. The areas below 225 μm^2 will be cut off.
2. The overlapping contours will only take the biggest bubbles as valid contours; others will be discarded.
3. The contour compactness below 0.4 will be discarded.

The first restriction is that the contour area below 225 μm^2 will be cut out because there are some contaminants on the CCD camera or small particles on the surfaces, which appear slightly darker than other regions and are detected as bubbles. Fortunately, the size

doi:10.6342/NTU202404416

of this outlier is usually very small, so we set a threshold value to cut off the smaller size contour as outliers.

The second restriction is concerned with the overlap of contours and the possibility of counting the same bubbles multiple times due to the overlap of the thick edge with low intensity. Since bubbles usually do not overlap but at most coalesce into one bigger bubble, we choose to select the larger, outer contour when two contours overlap.

The final restriction is about the contour compactness. We observed that the program sometimes detects some irregular shapes that are not consistent with what we observe as bubbles.

Therefore we add a constrain to select only those bubble contours that are compact enough. The compactness here is defined as the contour area divided by the smallest rectangle that can surround the contour. The definition is written in Equation 2.24, where A_{contour} means the area of contour and A_{rect} means the area of the smallest rectangle that can surround the contour.

$$\text{Compactness} = \frac{A_{\text{contour}}}{A_{\text{rect}}} \tag{2.24}$$

This definition deviates from the traditional one, which describes how circular one contour is. Since the bubbles here are usually not a perfect circle; but more like an ellipse, we would discard real bubbles with the traditional definition. The definition here is to see how a rectangle is a contour; if it is a perfect rectangle, the value of compactness will be one; as for a perfect circle, its compactness is close to 0.785. We set the threshold value for contour compactness above 0.4. Every contour with a compactness value lower than

doi:10.6342/NTU202404416

0.4 will be regarded as an outlier. This definition is good for depicting the outliers that are sharp, irregular, and long in shape.

However, one thing needs to be noted, the image analysis procedure here can only analyze the bubbles that escaped away from the confined slit. Because of the spatial and time resolution limits of our CCD camera, the bubbles within the confined region are only nano-meter thick and micro-meter wide, which is too blurry to characterize it with the CCD camera result. Fortunately, the FECO pattern is capable of dealing with such nano-meter scale characterization, and the bubble size in the confined region will be analyzed by the FECO pattern, which will be discussed in subsection 3.1.4.

As for the bubbles just flowing off the confined region, the flow rate is too fast that the CCD camera can only capture a trajectory of bubbles, which is still unable to do image analysis since the shape of the bubble is actually overlapping in the trajectory. As such, the image analysis here can only analyze the bubbles that fly a little farther away from the contact region and begin to show a stable oval shape that the program can capture.

The Python script, developed with the assistance of ChatGPT, enabled us to quickly analyze the *in-situ* videos. However, the conceptual framework for the analysis was our own innovation. The script is included in Appendix B.

doi:10.6342/NTU202404416

doi:10.6342/NTU202404416

Chapter 3 Result and Discussion

3.1 Confinement induced HER

3.1.1 The stability under different electrolyte conditions

The first step is to identify a suitable electrolyte. Sulfuric acid offers several advantages as an electrolyte, one of which is its ability to provide a high concentration of protons as reactants for the reaction. As a result, we chose sulfuric acid as the electrolyte. However, we encountered difficulties when deciding on the electrolyte concentration.

We tested three electrolyte pH conditions: pH0, pH3, and pH5 sulfuric acid aqueous solution by applying negative potentials on the electrode surface to initiate the hydrogen evolution process; meanwhile, we confined the electrode surface with the help of SFA. Surprisingly, all three pH conditions show that the hydrogen bubbles will generate from the center of the confined region, which is called confinement-induced HER. However, we also observed that the electrode surface suffers damage to different degrees during the hydrogen evolution process in pH3 and pH5 cases.

The reason for the hydrogen bubbles tearing off the gold surface may originate from the sandwiched structure of our electrode surface. Since the adhesion force between gold

doi:10.6342/NTU202404416

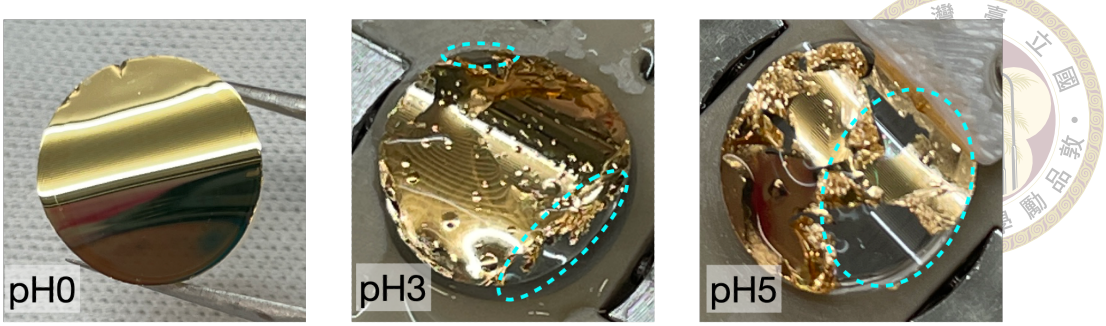

Figure 3.1: Photographs of the electrode surface condition after HER testing under electrolyte conditions of pH 0, pH 3, and pH 5. The dashed line indicates the region of surface damage. Note that the pH 3 and pH 5 images were taken while the surface was still wet, so droplets are visible on the surface.

and glass is so weak, a common way to deal with this problem is to use chromium or titanium as the adhesive layer between gold and glass. However, we didn't choose this strategy. Rather, we use optical glue as an adhesive layer to fix the gold on the glass disc, which is because we need an ultra-flat surface for SFA measurement, and the common way to prepare these kinds of surfaces is TSM (shown in subsection 2.3.2), while TSM needs to use optical glue to transfer the ultra-flat gold layer to the glass substrate.

Since the optical glue is a complex compound containing mercapto esters that can form strong bonds with gold, according to literature [49], the gold-sulfur bond will undergo a reduction reaction that will break the bond if a negative potential is applied [49]. For the larger pH cases, the potential needed to initiate the HER is more negative, falling in the potential window for Au-S bond reduction. That's why we observed that the HER on the electrode also ruined the surface.

SFA can help us measure the force-distance curve; by applying Derjaguin-Landau-Verwey-Overbeek (DLVO) fitting[50], we can get useful information about the electrode surface and the double layer structure of the interface, such as surface potential, surface charge, etc. However, the application of the DLVO model is limited to low electrolyte concentration[51] (to mimic the ideal solution). When the electrolyte concentration is too

doi:10.6342/NTU202404416

high, the DLVO model collapses and will have little usage since it deviates from the initial assumption of the model.

The hydrogen bubble also pushes the electrode away when it is generated, creating high fluctuations in separation distance (d_{sep}) that are visible as a big noise to the force measurement and make the DLVO fitting extremely hard to proceed with.

Therefore, we finally decided to sacrifice the double-layer information that SFA can provide and choose pH 0 sulfuric acid as the electrolyte condition for the experiments that were conducted. The reasons are as follows:

- The DLVO fitting is hard to achieve when the hydrogen is evolving, so it is not necessary to maintain low ionic strength (high pH) electrolyte conditions.
- Preparing the sample and setting up the SFA take a considerable amount of time. As a result, it is necessary to maintain the electrode surface condition after each measurement so that multiple experiments can be conducted with a single preparation.

3.1.2 Defects induced HER

Angulo *et al.* indicated that when the gas bubble evolves on the GEEs, defects on the electrode surface are the most likely location for bubbles to coalesce.[22] (also see Figure 1.5)

Using the SFA setup, we observed that the bubbles were generated from the confined area when the gold electrode and mica surface were brought into close proximity in a micrometer to the nanometer scale, and then negative polarization was applied.

Figure 3.2-(a) to (e) demonstrate the in-situ images of the gold electrode when it

doi:10.6342/NTU202404416

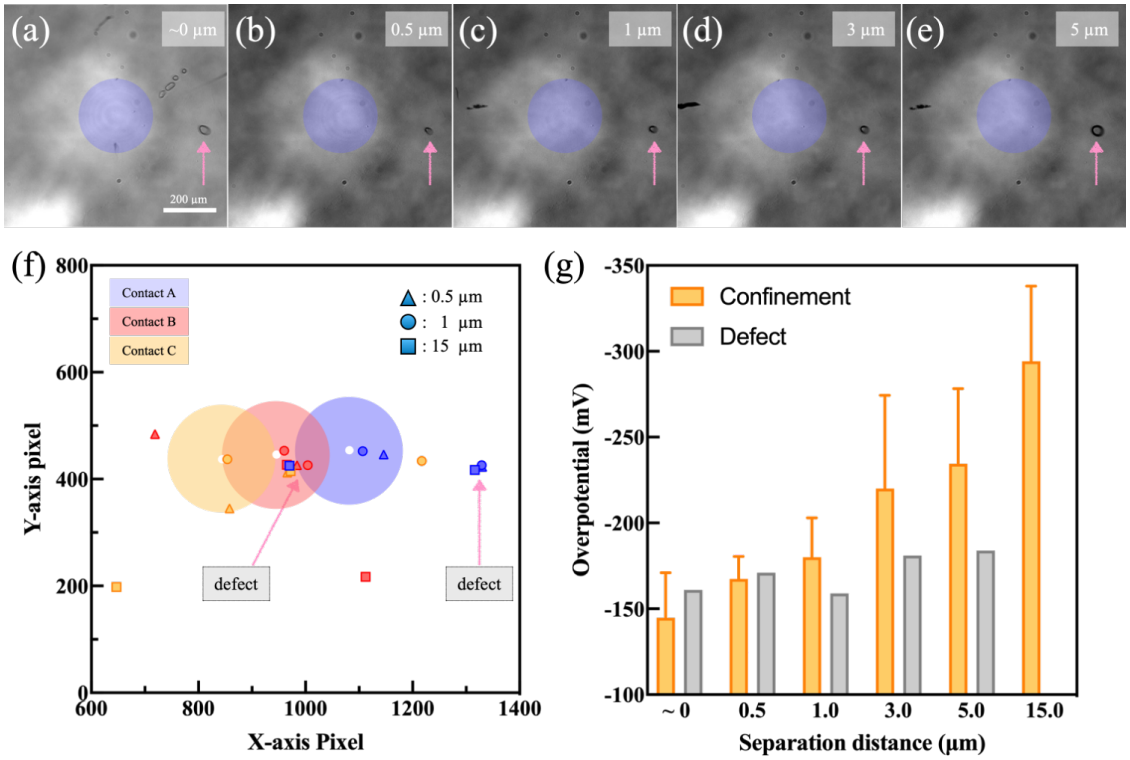

Figure 3.2: (a) to (e) is the bubbles generation process under different separation distances in-situ image snapshot, the pink arrows point out the location of defects. (f) the 2-D mapping of bubble formation locations under 0.5, 1, and 15 μm, compared with three different contact positions, the pink arrows indicated the position of defects, and the different shapes of data points represent three kinds of separation distances. The contact point is plotted in white dots for three different contact position. (g) The overpotential trends at different separation distances. Compare the trends with and without defects in the ROI. Note that there's no data for defects under 15 μm separation distance

doi:10.6342/NTU202404416

was undergoing negative polarization by LSV under different separation distances. The first evolved hydrogen bubble was observed in Figure 3.2- (b) to (e), and we found that it appeared at almost the same point (pointed by the arrow) regardless of the separation distances. We thought that this kind of spot might be the defect on the electrode, where bubbles are easier to coalesce. The result above indicated that the evolution spot is controlled by defects in these separation distances if the contact point of the mica and gold surface is too close to the defects. As for Figure 3.2-(a), the early bubble evolved in the center of the contact region when the separation distance was almost 0 micrometers; however, there were still some bubbles that evolved from the same defect, but not the first bubbles evolved from the electrode.

Another way to prove the influence of the defect site is to change different contact points on the WE by changing the back-silvered disc position relative to the fixed gold surface. If the coordinate of the bubble generation spot is independent of the contact point, then it may be a defect. We chose three different contact points on the WE surface to do the polarization at three different separation distances. The separation distance is controlled by first setting the two surfaces in contact and then driving the mica surface away through a piezo motor, which can give nanometer-scale resolution.

The result is shown in Figure 3.2-(f). The bubble generation points are represented in different colors to indicate the results from various contact points, while the shape of the data points represents the separation distances during the experiment. The three semi-transparent circles denote the Newton ring region, which is visible only when the separation distance is less than 1 micrometer. This feature serves as a useful tool to identify the contact point, as the contact point will be located at the center of the Newton ring. The contact points are plotted as white dots for the three contacts. After we plotted the

doi:10.6342/NTU202404416

locations where the first bubbles evolved from the electrode and identified several spots (indicated by pink arrows) where bubbles frequently evolved, we found that the spots remained prone to bubble formation even when the contact position changed, suggesting that the spots were independent of confinement. We hypothesize that these specific spots are defects on the electrode, where localized concentrations of dissolved hydrogen accumulate, facilitating hydrogen evolution at these positions.

We also analyzed the overpotential needed for the WE to generate hydrogen and evolve the first bubble, which is captured by the in-situ video. The result is shown in Figure 3.2-(g). For those sites that contain defects visible in the microscope, we found that the small overpotential necessary for HER is independent of the separation distance.

The overpotential is largely reduced compared to the result obtained from regions of interest (ROI) that do not include defect sites (this result will be further discussed in subsection 3.1.3), which may cause a serious outlier issue.

As a result, for the experiment below, we will only use the 600 x 600-pixel area centered around the contact (although the CCD camera can capture 1440x1080 pixels) to do image analysis, preventing the outliers from affecting the experimental result. Another advantage of lowering the capture area is that the lower area can provide higher frames per second (FPS), which enables us to get higher time resolution in in-situ videos.

To counteract the effects of defects, we are also careful when preparing the surfaces for the experiment and choose a relatively flat region on the CCD to prevent defects when choosing the contact position. If the defect is accidentally contained in the ROI, we will drop off the whole set of data received from that contact position. In this way, we can minimize the influence of defect-induced HER and focus on confinement-induced HER.

doi:10.6342/NTU202404416

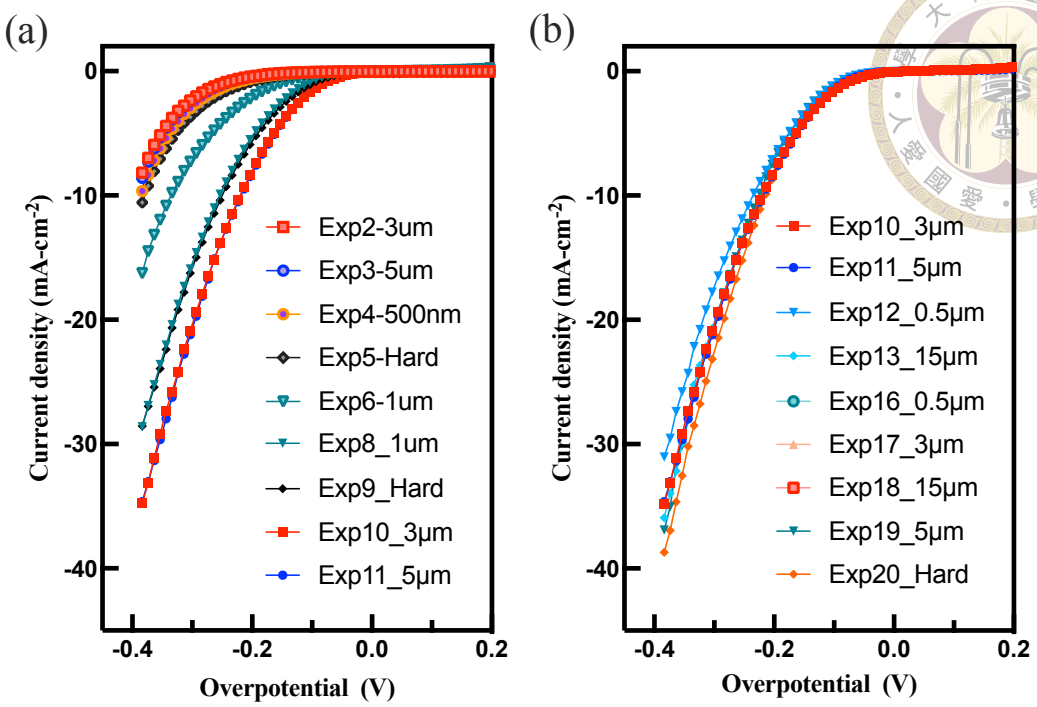

Figure 3.3: The voltamogram got by linear scan the working electrode from 0.2 V to -0.4 V under 0, 0.5, 1, 3, 5, 15 μm separation distances. The series of separation distances that chose to conduct the experiment is randomly choosing. (a) The curves show an increasing trend of the current density value with the increase trials of experiment. (b) The curves show current density maintain a similar trend regardless of the separation distances.

3.1.3 Distance dependency of HER overpotential

Using the LSV technique and SFA setup, our original goal was to investigate the correlation between separation distance (d_{sep}) and the HER overpotential at 10 mA/cm² using voltammograms. The LSV data is presented in Figure 3.3. Figure 3.3-(a) shows the LSV curves from experiments two through eleven, reflecting the experimental progress under varying separation distances (hard contact, 0.5 μm, 1 μm, 3 μm, 5 μm, 15 μm). Since we conducted all experiments using the same surface and electrolyte over different separation distances, it was crucial to ensure that the data we obtained was only influenced by the parameter we were testing, i.e., the separation distance, and not by any variations in the surface or electrolyte over the course of the experiments. To achieve this, the order of the separation distances was chosen randomly to determine whether the

doi:10.6342/NTU202404416

differences in the LSV data were directly affected by the separation distance, which also represents the degree of confinement. Surprisingly, the current density displayed an increasing trend across the first eleven experiments, regardless of separation distance, as shown in Figure 3.3-(a). When we continued performing linear scans, we observed that the current remained steady, unaffected by separation distance, as shown in Figure 3.3-(b). These results indicate that the current density gradually increases over successive scans of the electrode surface and eventually reaches a steady state. This phenomenon can be attributed to the relatively small confinement area (approximately 300 μm^2) [52], which is negligible compared to the total working electrode area (around 83 mm^2). Since the contact area is so small, it contributes an insignificant portion of the total current, limiting the electrochemical information we can obtain from the LSV voltammograms, as the current from the contact area represents only a small fraction of the total current. The lack of hydrogen generation outside the confinement area, despite the current contribution, could be due to oxygen generation at the CE. The oxygen may diffuse and adsorb onto the WE, where it is reduced to water as the WE is negatively polarized, contributing to the current. However, we were unable to observe water generation under the microscope due to limitations of the CCD. Therefore, the LSV voltammograms cannot provide useful insights into confinement-induced HER, as the voltammetry plots under different confinement conditions show little correlation with d_{sep}.

As a result, we turned to using the LSV technique to toggle the applied potential while recording the HER through a CCD camera at different separation distances. While the current measured from the electrochemical measurement does not show a clear trend, we observed a correlation between the separation distance and the overpotential needed to evolve the first bubble. Conducting the above data analysis method for different d_{sep},

doi:10.6342/NTU202404416

we got the trends of evolution overpotential shown in Figure 3.2-(g). The overpotential needed to initiate HER is gradually decreased as the d_{sep} decreases, which shows that the confinement indeed possesses the catalytic ability toward HER, and the lower the separation distance, the higher the catalytic ability.

Traditionally, confinement effects are usually defined as effects induced by nanometer scale confinement[53]. However, in our experiment, we found that the evolution potential does not show a difference when the separation distance is set to be nanometer scale. So we increased the separation distance and found that the trends in evolution potential and separation distance occurred when the separation distances reached the micrometer scale.

As for why there's little difference in evolution potential under different separation distances on a nanometer scale, we thought that it might be because the confinement will be distorted when the hydrogen bubbles start to evolve. The hydrogen bubble will keep pushing the mica surface away, so the mica surface will act as a seesaw and keep moving back and forth, which makes the separation distance show a huge error in the nanometer scale. Consequently, we are not able to control the separation distance on a 0.1 nanometer scale when the HER starts to proceed. Hence, we only set one separation distance in a nanometer scale, the hard contact, which means the two surfaces are attached to each other, and the separation distance will become 2 to 3 nano-meters since there will also be few layers of molecules that are sandwiched by the two surfaces and be trapped there.

From the confinement-induced HER trends shown in Figure 3.2-(g), we can deduce two kinds of factors guiding the reaction.

- short-range influence: this only affects the reaction at a few nanometers separation

doi:10.6342/NTU202404416

distance (Hard contact)

- long-range interaction: triggers the reaction at micrometer scale confinement

3.1.4 Capture of HER within a nanometer-confined gap

By utilizing our home-designed EC-SFA, we establish a hard confinement between a gold working electrode surface and a back-silvered mica surface. We successfully trigger the HER within the confined gap by ramping the potential towards negative polarization, as shown in Figure 3.4-(a). Through the time-resolve FECO analysis in Figure 3.4-(a), we observe an early-stage nano-scale bubble formation within the gap with a lifetime of 1 second, where the observed bubble is in a size of the radius of about 10 μm and thickness of 3 nm as shown in Figure 3.4-(b).

After the first bubble reaches its maximum size, it disappears within 0.1 seconds by creating a nano-channel at the left-hand side with a height of about 0.8 nm as indicated in Figure 3.4-(b). About 0.5 seconds after the first bubble event, the same hot spot quickly generates the second bubble, which grows to a similar size as the first one. Similarly, the second bubble escapes from contact through the nearby nano-channels, as can be compared with the first one in Figure 3.4-(a) and (b).

Different from the first event, the reaction intensity of the second event is getting stronger along with the increase of the overpotential, where we observe a very significant gap swelling within the contact. As the reaction progresses, the bubble's lifetime gets shorter; meanwhile, the gap swelling goes up to nearly 5 nm, providing more nano-channels to accelerate the gas exhaust. The event of gas trapping is very pronounced and is visible directly from the pattern of FECO as shown in Figure 3.4-(c), where the dashed

doi:10.6342/NTU202404416

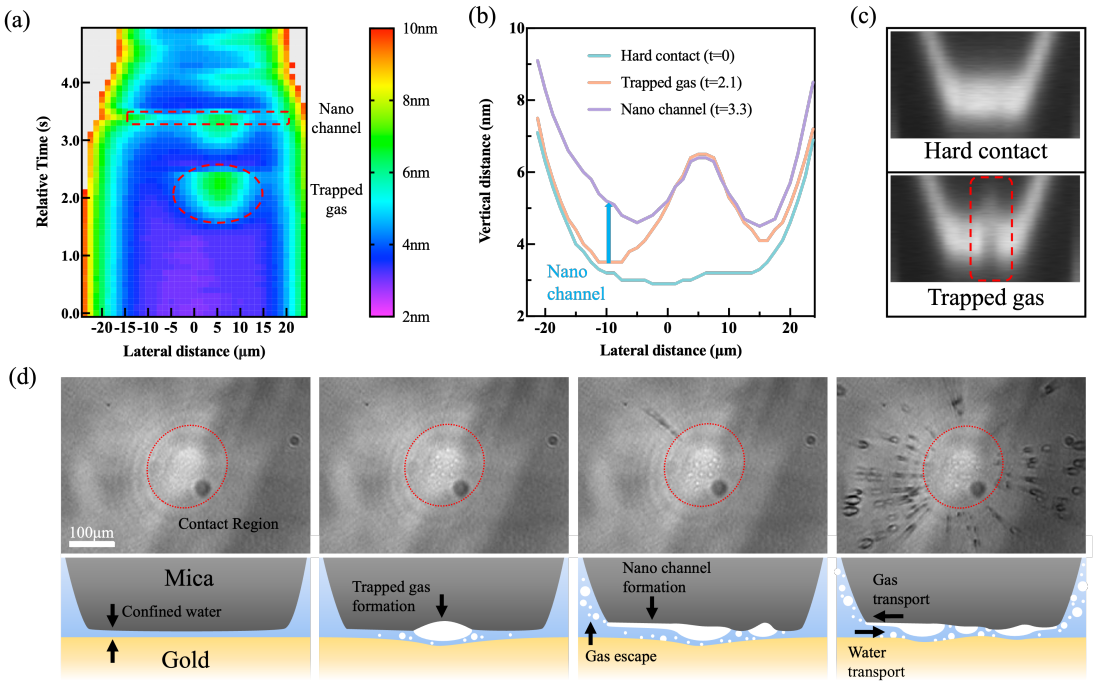

Figure 3.4: Time-resolved contact geometry analysis at the initial stage of HER. (a) SFA gap separation analysis upon the initiation of HER within the confinement, where the separation distances are marked by colors. (b) Cross-section analysis of the contact taken at t = 0.0, 2.1, and 3.3 s from the relative time scale of (a), respectively. (c) Comparison of FECO with and without gas bubble trapped. (d) Macroscopic 2D optical images taken from different stages of HER within the confined region.

doi:10.6342/NTU202404416

line indicates there's a bubble inside the confinement region.

To gain an overview of the 2D HER bubble formation in the CCD view, we remove the 532 nm bandpass filter, allowing for NR capture, after acquiring the contact position from the NR. With the full view, screenshots taken from the camera shown in Figure 3.4-(d) reveal the progress of bubble formation from the contact area (marked in dash red circle).

Following the applied potential increase, the gas bubble formation is first observed within the confined contact region, as illustrated, which deforms the contact slightly. With the growth of the bubble, the one near the edge of the contact establishes a nano-channel to exhaust the pressurized gas within the contact. Interestingly, gas exhaust seems to be a continuous process that forms a non-stop gas stream, as captured by the camera. At very high polarization, bubble formation becomes very active where multiple gas streams are established, which all originate from the confined area.

These streams not only provide a pathway to let the hydrogen bubble escape from the confinement area but also stir the electrode surface and allow the bulk solution to transport into the confinement area, which may be strong evidence that can explain why the hydronium ion will not be consumed up and stop the reaction.

3.2 Possible reasons for confinement induced HER

In this section, we are elaborating on the possible reasons for the confinement-induced HER phenomena. Below, we put our measurement and simulation results in the context of four proposed reasons leading to the confinement-induced HER effect.

doi:10.6342/NTU202404416

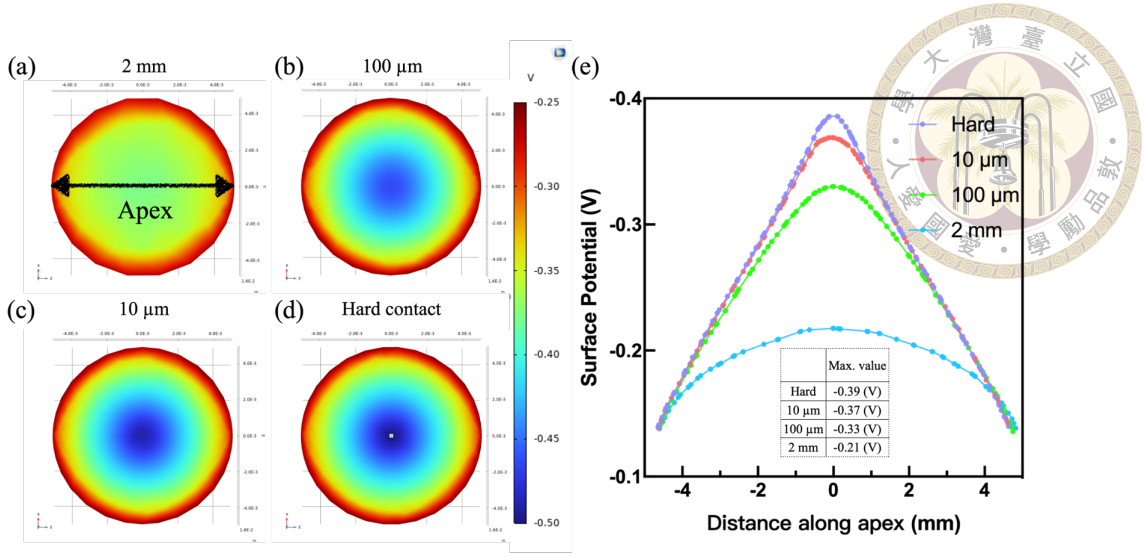

Figure 3.5: Surface potential distribution on the WE under different d_sep. (a) to (d): d_{sep} is 2 mm, 100 μm, 10μm, 0 μm (hard contact) (e) The surface potential distribution alone the apex under different d_{sep}, the inset table shows the peak voltage value which is roughly located in the middle of the apex

3.2.1 The uneven distribution of electrode potential under confinement

Dziadkowiec *et al.* successfully used SFA setup to catalyze calcite growth under confinement conditions; one of the reasons they explain such confinement effect is the uneven electric potential on the surface when the surface is polarized by certain overpotential.[54]

Inspired by this discovery, we use Comsol Multi-physics to try to model the surface potential on the gold surface when applying -0.6 V on the gold surface and compare the potential distribution under four different separation distances, which are 0 μm, 10 μm, 100 μm, and 2 mm. In this geometry, 0 μm means the two surfaces are in complete contact with each other, denoted as Hard contact, while the 2 mm is the largest distance that the SFA surfaces can be separated, which can be simplified as totally separated to model the free space condition.

The result can be seen in Figure 3.5 which shows that the center part of the disc

doi:10.6342/NTU202404416

always exhibits larger absolute values of surface potential even at high separation distances; the reason for this phenomenon is because the electrode itself is not a flat surface, but a curved surface where the radius of curvature is 1 cm. The electronic repulsion force between free electrons will make electrons gather close to the high curvature area[55]; this explains why we always see the contact point exhibiting the highest potential values. Apart from that, we can see that the potential shows a positive deviation from the given potential (-0.6 V); the reason for this is because of the screening effect of the high electrolyte concentration of 0.5 M sulfuric acid. The sulfuric acid can screen the potential value on the surface since the Deybe length at this condition is less than 1 nanometer.

From Figure 3.5-(a) to (d), we found that the confinement indeed altered the potential distribution on the electrode surface. The closer the surfaces are, the larger the absolute value of surface potential is. We also draw a 1-D line graph to show the surface potential distribution along the apex, which is the highest line of a cylindrical surface. In hard contact, the surface potential is more negative compared to the condition at 2 mm separation, with a potential difference of almost 200 mV. This is strong evidence that confinement-induced HER is linked to the uneven distribution of potential on the electrode surface. From a mass-transport point of view, confinement affects the potential distribution and hence affects the migration of ions in the electrolyte, making protons more willing to come to the WE.

Nevertheless, the model here only assumes that the mica is an insulated surface, which does not consider the surface charge of the mica surface since it'll need to couple the surface charge physics field in the modeling, which is hard to complete. As a result, the result demonstrated here is saying that the uneven distribution is not mica specific; rather, it happens when an insulated surface confines the WE.

doi:10.6342/NTU202404416

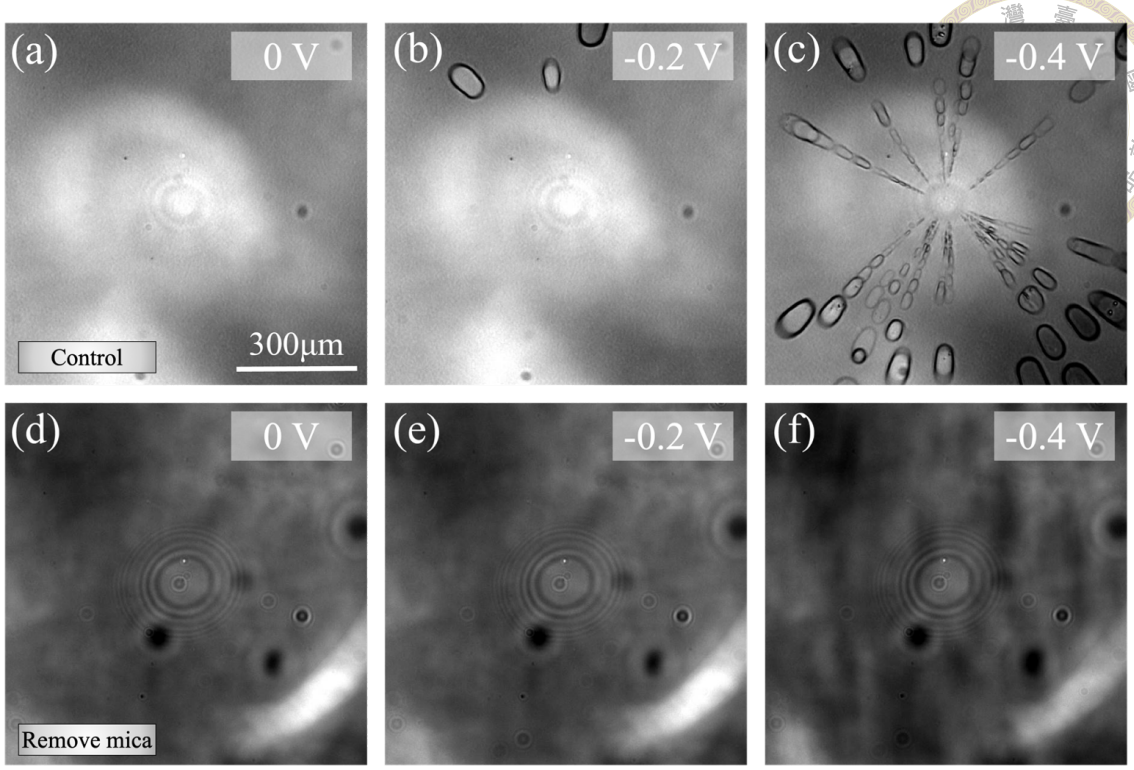

Figure 3.6: In-situ image captured at different overpotentials under Hard contact, (a) to (c): gold vs. mica; (d) to (f) gold vs. optical glue. (a)(d) is 0 V vs. RHE (b)(e) is -0.2 V vs. RHE (c)(f) is -0.4 V vs. RHE

3.2.2 The presence of Muscovite mica surface

The Muscovite mica surface contains plenty of potassium ions as K^+ dissociates from the interface when placed in solution, leaving behind a net negative charge on the mica. In our experiment, mica is exposed to the 0.5 M sulfuric acid, accumulating positively charged protons in its double layer to screen out the negative charge on the mica surface.

Given the high proton concentration on the mica interface, our hypothesis for confinement driven HER entails the mica increasing the proton concentration on the Au when the mica and gold surfaces come close enough. The higher proton concentration near the electrode surface facilitates the HER happening at lower overpotentials.

To verify this assumption, we prepared two sets of surfaces: one is gold vs. mica, and another is gold vs. optical glue, which functions as a reference experiment. We conducted

doi:10.6342/NTU202404416

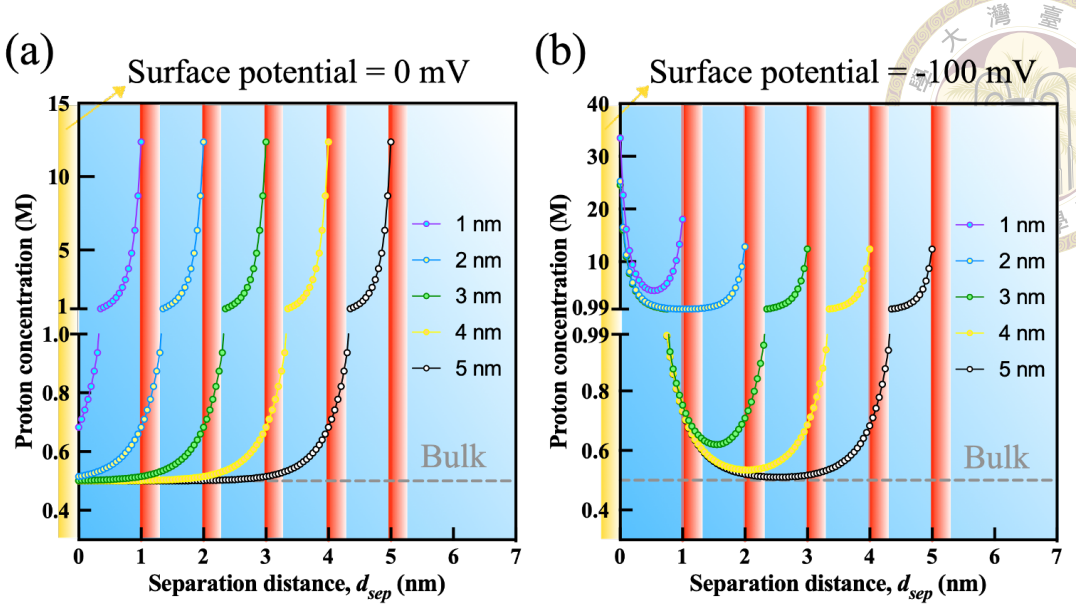

Figure 3.7: The proton concentration profile at different separation distances under (a) 0 mV and (b) -100 mV surface potential set on the gold surface. The yellow rod at the left-hand side of the (a) and (b) indicate the gold surface, while the red rod symbolize the mica surface, which is set away from the gold surface at 1, 2, 3, 4, 5 nm, respectively.

LSV at separation distances of 0 μm (Hard contact). In Figure 3.6, we found that the surfaces prepared with just optical glue showed no confinement-driven reaction in the ROI, while the mica-bearing surface started generating hydrogen bubbles near the contact point at around -0.19 V vs. RHE.

This observation provides strong evidence that the mica surface plays an important role in the confinement-driven HER, and the reaction is mica-specific. It is not simply induced by surface confinement; rather, it is the confinement between mica and gold that allows confinement-induced hydrogen evolution reaction to occur.

3.2.2.1 Python modeling of the proton concentration profile

Comsol-Multiphysics is a mature commercial software that allows the user to deal with the modeling process in a very simple way. However, it also makes it hard to understand the error message and overcome the errors, especially when we try to couple

doi:10.6342/NTU202404416

multiple physics fields in one model.

As a consequence, we turn to use a self-coded Python script (attached in Appendix A) for modeling the 1-dimensional proton concentration profile when the gold surface is confined by the mica surface and compared two conditions: one is the gold electrode under no additional external polarization, and the other is the gold electrode set at a surface potential of -0.1 V. These two conditions simulate the situation when the gold and mica are confined and reach an equilibrium with the electrolyte. When the gold electrode is under a negative potential, it will adsorb positively charged protons accumulating on the electrode surface. One thing that needs to be noticed is that the model here considers there's only a proton in the system; we neglect the influence of counter ions, which may, hence, induce a small deviation from the real-world cases. We just want to see the trends when the separation distance is varied.

The result is shown in Figure 3.7; the red rod symbolizes the mica surface, and the gold rod symbolizes the gold surface. We tested five separation distances between gold and mica surfaces, which are 1, 2, 3, 4, and 5 nm, respectively.

Distance (nm)	Surface Potential = 0 mV	Surface Potential = -100 mV
1	0.683159	33.48667
2	0.515417	25.26437
3	0.501480	24.58120
4	0.500144	24.51572
5	0.500014	24.50936

Table 3.1: Proton surface concentration at different separation distances

We found that the screening effect from 0.5 M sulfuric acid indeed plays a crucial role, making the concentration gradient unable to reach far into the solution. However, the proton concentration on the gold surface (shown in Table 3.1 indeed shows a slight increase when the separation distances are set to be 1 nm for no applied potential cases.

doi:10.6342/NTU202404416

For surface potentials of -100 mV cases, the surface proton concentration (shown in Table 3.1) at 1 nm separation even shows a dramatic increase to about 33 M on the gold electrode surface. We also found that although the surface proton concentration only shows a significant difference in 1 nanometer, 2 $\sim$ 4 nanometers confinement also shows that the proton concentration in the confined area will be larger than bulk concentration, so after the HER consumes the surface proton concentration, these confined regions can provide more proton concentration compared with bulk solution can provide.

These simulations reveal that the mica surface indeed increases the proton concentration within 4 nm separation distance, which may provide an explanation for why the hard contact cases show the smallest overpotential for confinement-induced HER, and the reason is regarded as the diffusion of protons from the mica surface. However, for other conditions in Figure 3.2-(g), we can only say that the micro-meter scale separation distance is not affected by the mica surface. The evidence from the proton concentration profile still cannot find a conclusive explanation as to why there's confinement-induced HER shown in the micro-meter scale.

In the next section, we try to provide some reasonable explanations to explain the micro-scale confinement effect.

3.2.3 Minimizing bubble size by confinement

In Figure 1.6, we discuss the overpotential induced by bubbles. However, they didn't further discuss how the size of the bubbles detaching from the electrode affects the performance of GEEs

Lu *et al.* has investigated how the bubble size affects the electrochemistry behav-

doi:10.6342/NTU202404416

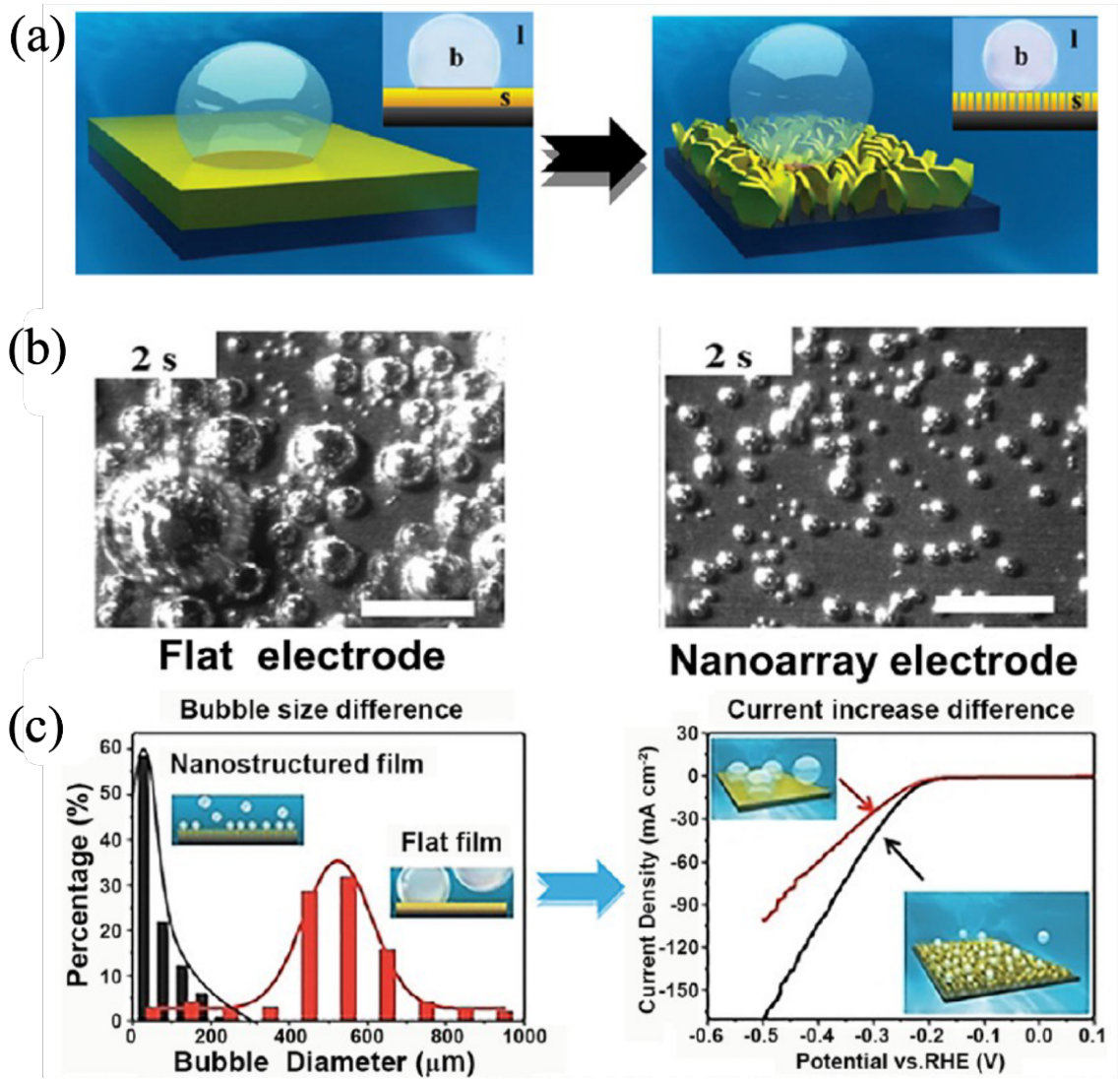

Figure 3.8: (a) Diagram illustrating bubble adhesion phenomena on flat electrode surfaces (left) and nanoarray electrode surfaces (right). (b) Representative images of bubbles on a MoS_2 nanostructured electrode (right) and a flat electrode (left). (c) Statistical analysis of bubble sizes upon detachment on both types of electrodes, along with the corresponding polarization curves.

doi:10.6342/NTU202404416

ior by comparing a flat substrate and a nano-arrayed substrate[56], and the reaction they investigate is also the HER. The result of their work is shown in Figure 3.8[21, 56]. Figure 3.8[21, 56]-(a) shows the schematic diagram of their sample morphology. By changing the flat MoS_2 surface into a nano-structured surface, they successfully reduced the bubble size on the electrode, as can be seen in Figure 3.8[21, 56]-(b).

They further did statistical research about the bubble radius distribution, Figure 3.8[21, 56]-(c) shows that the bubbles on the nano-structured surface will depart from the surface usually below 100-micrometer radius, which is considerably smaller than that of the flat surface. The corresponding LSV voltammogram of these two surfaces is also discussed in Figure 3.8[21, 56]-(c); it shows that the nano-structured surface can enhance the current density at the same overpotential compared with the flat electrode. The result above demonstrates that the bubble size did play a crucial role in HER performance.

The result of Lu *et al.* makes us think about whether the confinement also alters the bubble behaviors. In our experiment, we observed that the in-situ video shows that when the surfaces are well-separated (about 2 mm), the hydrogen bubbles will adsorb on the electrode surface for a very long time, growing to a large size and then departing, as we can see in Figure 3.9[57]-(a). As for the micro- and nano-confinement cases, the generated bubbles can not stay too long on the electrode surface; they would rather deform and burst into plenty of tiny microbubbles as illustrated in the Figure 3.9[57]-(b) since the height of the bubble is restrained by the separation distance.

This may provide a reasonable explanation for the evolution overpotential trends we have discussed in Figure 3.2-(g), in which we proposed that the confinement-induced HER is dominated by short-range and long-ranged interaction. In our experiment, we observed

doi:10.6342/NTU202404416

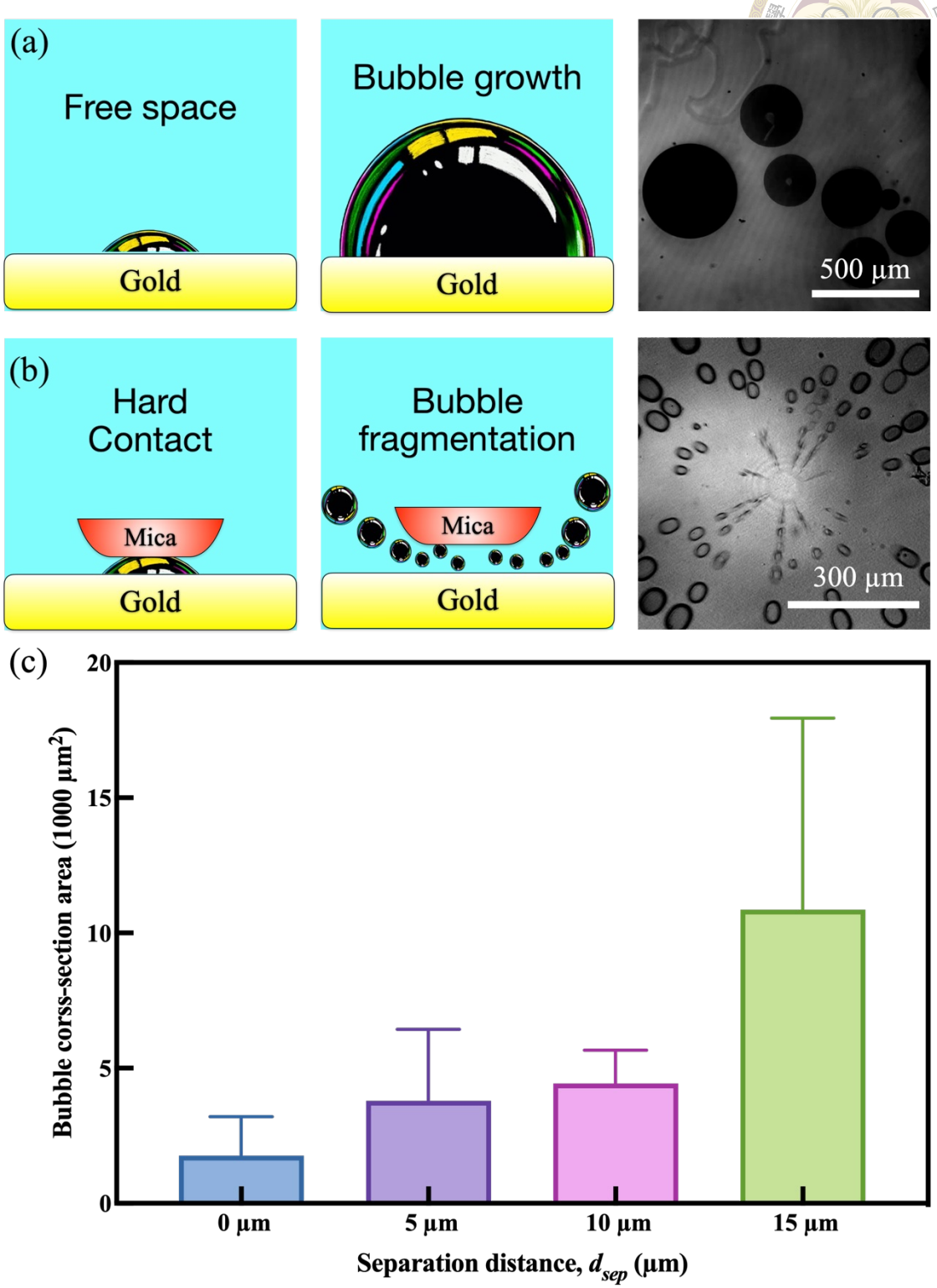

Figure 3.9: (a) The schematic diagram of the bubble growth mechanism in free space, and there is an in-situ image as evidence. (b) In the bubble growth mechanism under confinement, the bubble's height is limited by the separation distance and will break into frictions in a short time. (c) The statistical data of the bubble cross-section area increased as the separation distance increased. The schematic picture of bubbles is taken from

doi:10.6342/NTU202404416

that the microbubble's radius varied at different separation distances based on the top view in-situ video.

In order to provide a quantitative analysis of the in-situ video, we used our developed Python script (attached on Appendix. B) to capture the bubble cross-section area visible in the top view in-situ video during the LSV potential scan. The result of the bubble cross-section area at different separation distances is summarized in the bar chart in Figure 3.9[57]-(c). The result in Figure 3.9[57]-(c) shows that the bubble size during the HER will be increased as the separation distance increases. This trend correlates well with the overpotential trends shown in Figure 3.2-(g). Hence, the overpotential is partially controlled by the bubble size, which affects the confinement-induced HER on a micrometer scale, contributing to both short- and long-range influence. From the bubble overpotential point of view, the lowering of bubble detachment size can also lower the bubble overpotential as we discussed in subsection 1.3.2. From the mass-transport point of view, the bubbles provide a convection effect to pump the protons to the confined area, and the lower the bubble size may make the convection effect higher.

3.2.4 Local concentrated effect on dissolved hydrogen

Another hypothesis for long-range interaction that needs to be mentioned is the local concentrated effect. In subsection 1.3.1, we have discussed the mechanism for a bubble to evolve. When the HER starts to generate hydrogen, it first dissolves into the electrolyte. Once the electrolyte becomes supersaturated with dissolved hydrogen near the electrode, the hydrogen bubble starts to nucleate and grow. We noted that the defect is more likely to generate hydrogen bubbles since the local hydrogen concentration is higher at the defect, making it easier to reach the supersaturated state.

doi:10.6342/NTU202404416

In our experiment, our method to decide the evolution potential is by observing visible hydrogen bubbles. However, before the visible microbubble starts to evolve and is captured by a CCD camera, the electrode must have evolved super tiny nanobubbles dissolved in the electrolyte. We assumed that when the electrode started to produce the hydrogen nanobubbles across its entire surface, the confined region may exhibit a higher concentration of dissolved hydrogen, thus producing the hydrogen microbubble that is only visible in the confined region. The local concentrated effect may be another perspective on the long-range interaction toward confinement-induced HER. However, this hypothesis has not yet been verified, and further research is needed to determine its validity.

doi:10.6342/NTU202404416

doi:10.6342/NTU202404416

Chapter 4 Conclusion

In summary, utilizing the SFA setup creating a well defined confinement between gold and mica surfaces, we successfully observed confinement-induced HER phenomena, even at separation distance on a micro-meter scale.

Considering the consumption of protons during the reaction, mass transport in a confined environment is of great concern. From the perspective of the Nernst-Plank equation (Equation 2.15), we try to answer how the proton transport into the confined gap can be achieved in three ways.

- Migration: With the help of Comsol multiphysics, we successfully model the potential distribution on the working electrode and find that the shorter the separation distance, the higher the potential values on the surface, leading to a migration of charge into the confined center along the potential gradient.
- Convection: The SFA setup functions in a stationary environment, which means there is no additional convection in this system. However, we use FECO analysis to find that there will be some micro convection due to the formation of bubbles, which induce the fast transportation of electrolytes into the gap and make the proton in the slit won't be consumed.
- Diffusion: From the Poison-Boltzmann equation, we can solve the high proton con-

doi:10.6342/NTU202404416

centration profile near the mica surface. If the EDL of mica and gold surfaces overlap, the high concentration of the proton can diffuse from the mica EDL to the gold surface, enhancing the proton's transportation ability.

All the factors above describe a short-range interaction, which cannot explain why the confinement at the micro-meter scale also shows catalytic ability. Therefore, some long-range interactions are in play that need further investigation.

We provide two possible explanations for the long-range interaction. One is that the confinement minimizes the size of the detached bubbles, which lowers the overpotential arising from them and hence lowers the total overpotential. Another reason is that the confinement region may show a higher concentration of dissolved hydrogen gas, thus making it easier to grow bubbles in the confined gap. However, the results for analyzing long-range interaction need further work and will be part of future research.

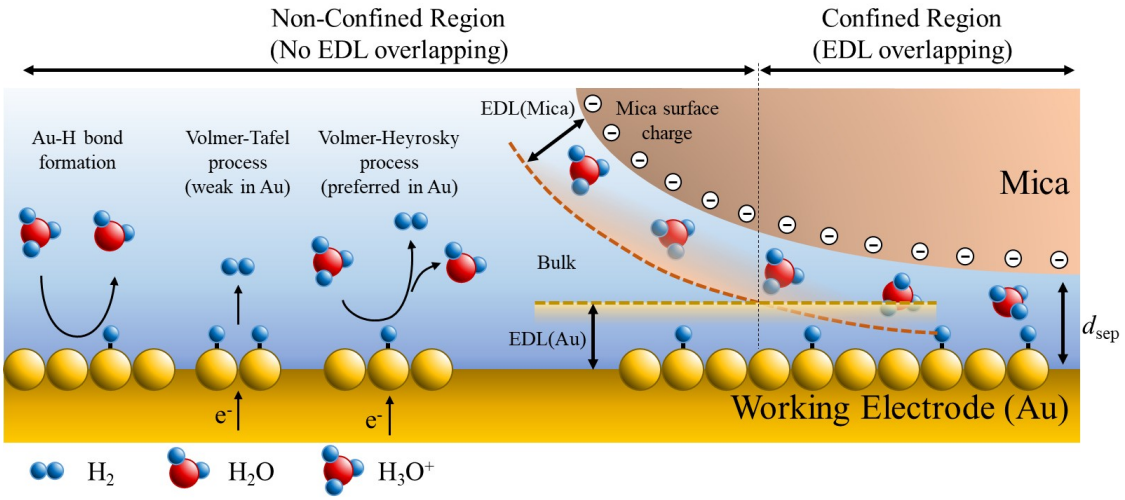

Figure 4.1: Schematically illustration of the EDL overlapping through confinement

doi:10.6342/NTU202404416

References

[1] Bassma Reda, Amr A Elzamar, Shehab AlFazzani, and Shahira M Ezzat. Green hydrogen as a source of renewable energy: a step towards sustainability, an overview. Environment, Development and Sustainability, pages 1–21, 2024.

[2] Mrinmoy Kumar Sarmah, Tej Pratap Singh, Pankaj Kalita, and Anupam Dewan. Sustainable hydrogen generation and storage–a review. RSC advances, 13(36):25253–25275, 2023.

[3] Marian Chatenet, Bruno G Pollet, Dario R Dekel, Fabio Dionigi, Jonathan Deseure, Pierre Millet, Richard D Braatz, Martin Z Bazant, Michael Eikerling, Iain Staffell, et al. Water electrolysis: from textbook knowledge to the latest scientific strategies and industrial developments. Chemical Society Reviews, 51(11):4583–4762, 2022.

[4] Guoqiang Zhao, Kun Rui, Shi Xue Dou, and Wenping Sun. Heterostructures for electrochemical hydrogen evolution reaction: a review. Advanced Functional Materials, 28(43):1803291, 2018.

[5] Carlos G Morales-Guio, Lucas-Alexandre Stern, and Xile Hu. Nanostructured hydrotreating catalysts for electrochemical hydrogen evolution. Chemical Society Reviews, 43(18):6555–6569, 2014.

[6] Aleksandar R Zeradjanin, George Polymeros, Cigdem Toparli, Marc Ledendecker,

doi:10.6342/NTU202404416

Nejc Hodnik, Andreas Erbe, Michael Rohwerder, and Fabio La Mantia. What is the trigger for the hydrogen evolution reaction?–towards electrocatalysis beyond the sabatier principle. Physical Chemistry Chemical Physics, 22(16):8768–8780, 2020.

[7] Akakuru Ozioma Udochukwub and Thomas Odey Magub. Understanding the mechanism of electrochemical reduction of co2 using cu/cu-based electrodes: a review. Asian Journal of Nanoscience and Materials, 1(4):183–224, 2018.

[8] Charles CL McCrory, Suho Jung, Jonas C Peters, and Thomas F Jaramillo. Benchmarking heterogeneous electrocatalysts for the oxygen evolution reaction. Journal of the American Chemical Society, 135(45):16977–16987, 2013.

[9] Hideshi Ooka, Jun Huang, and Kai S Exner. The sabatier principle in electrocatalysis: Basics, limitations, and extensions. Frontiers in Energy Research, 9:654460, 2021.

[10] Sami M Ibn Shamsah. Earth-abundant electrocatalysts for water splitting: current and future directions. Catalysts, 11(4):429, 2021.

[11] Subhasis Shit, Saikat Bolar, Naresh Chandra Murmu, and Tapas Kuila. An account of the strategies to enhance the water splitting efficiency of noble-metal-free electrocatalysts. Journal of Energy Chemistry, 59:160–190, 2021.

[12] Sebastien Rauch and Olalekan S Fatoki. Impact of platinum group element emissions from mining and production activities. In Platinum metals in the environment, pages 19–29. Springer, 2014.

[13] Yulin Sun, Chuanqi Huang, Junling Shen, Yijun Zhong, Jiqiang Ning, and Yong Hu. One-step construction of a transition-metal surface decorated with metal sulfide nanoparticles: A high-efficiency electrocatalyst for hydrogen generation. Journal of colloid and interface science, 558:1–8, 2020.

doi:10.6342/NTU202404416

[14] Yanmei Shi and Bin Zhang. Recent advances in transition metal phosphide nanomaterials: synthesis and applications in hydrogen evolution reaction. Chemical Society Reviews, 45(6):1529–1541, 2016.

[15] Yi Shi, Yue Zhou, Dong-Rui Yang, Wei-Xuan Xu, Chen Wang, Feng-Bin Wang, Jing-Juan Xu, Xing-Hua Xia, and Hong-Yuan Chen. Energy level engineering of mos2 by transition-metal doping for accelerating hydrogen evolution reaction. Journal of the American Chemical Society, 139(43):15479–15485, 2017.

[16] Ashish Kumar and Venkata Krishnan. Vacancy engineering in semiconductor photocatalysts: implications in hydrogen evolution and nitrogen fixation applications. Advanced Functional Materials, 31(28):2009807, 2021.

[17] Jinbong Seok, Jun-Ho Lee, Suyeon Cho, Byungdo Ji, Hyo Won Kim, Min Kwon, Dohyun Kim, Young-Min Kim, Sang Ho Oh, Sung Wng Kim, et al. Active hydrogen evolution through lattice distortion in metallic mote2. 2D Materials, 4(2):025061, 2017.

[18] Jing-Fang Huang, Ruo-Hua Zeng, and Jeng-Lung Chen. Thermostable carbon-supported subnanometer-sized (< 1 nm) pt clusters for the hydrogen evolution reaction. Journal of Materials Chemistry A, 9(38):21972–21980, 2021.

[19] H Vogt. The voidage problem in gas-electrolyte dispersions. Journal of applied electrochemistry, 17(2):419–426, 1987.

[20] MG Fouad and GH Sedahmed. Mass transfer at horizontal gas-evolving electrodes. Electrochimica Acta, 18(1):55–58, 1973.

[21] Mengxuan Li, Pengpeng Xie, Linfeng Yu, Liang Luo, and Xiaoming Sun. Bub-

doi:10.6342/NTU202404416

ble engineering on micro-/nanostructured electrodes for water splitting. ACS nano, 17(23):23299–23316, 2023.

[22] Andrea Angulo, Peter van der Linde, Han Gardeniers, Miguel Modestino, and David Fernández Rivas. Influence of bubbles on the energy conversion efficiency of electrochemical reactors. Joule, 4(3):555–579, 2020.

[23] Yi He, Yifan Cui, Wenxu Shang, Zhongxi Zhao, and Peng Tan. Insight into the bubble-induced overpotential towards high-rate charging of zn-air batteries. Chemical Engineering Journal, 448:137782, 2022.

[24] John Dukovic and Charles W Tobias. The influence of attached bubbles on potential drop and current distribution at gas-evolving electrodes. Journal of the Electrochemical Society, 134(2):331, 1987.

[25] Yi He, Yifan Cui, Zhongxi Zhao, Yongtang Chen, Wenxu Shang, and Peng Tan. Strategies for bubble removal in electrochemical systems. Energy Reviews, 2(1):100015, 2023.

[26] Tatsuki Fujimura, Wakana Hikima, Yasuhiro Fukunaka, and Takayuki Homma. Analysis of the effect of surface wettability on hydrogen evolution reaction in water electrolysis using micro-patterned electrodes. Electrochemistry Communications, 101:43–46, 2019.

[27] Ryuichi Iwata, Lenan Zhang, Kyle L Wilke, Shuai Gong, Mingfu He, Betar M Gallant, and Evelyn N Wang. Bubble growth and departure modes on wettable/non-wettable porous foams in alkaline water splitting. Joule, 5(4):887–900, 2021.

[28] C Gabrielli, F Huet, M Keddam, A Macias, and A Sahar. Potential drops due to an

doi:10.6342/NTU202404416

attached bubble on a gas-evolving electrode. Journal of applied electrochemistry, 19(5):617–629, 1989.

[29] Amir Taqieddin, Roya Nazari, Ljiljana Rajic, and Akram Alshawabkeh. Physicochemical hydrodynamics of gas bubbles in two phase electrochemical systems. Journal of The Electrochemical Society, 164(13):E448, 2017.

[30] Valentina Wieser, Pierluigi Bilotto, Ulrich Ramach, Hui Yuan, Kai Schwenzfeier, Hsiu-Wei Cheng, and Markus Valtiner. Novel in situ sensing surface forces apparatus for measuring gold versus gold, hydrophobic, and biophysical interactions. Journal of Vacuum Science & Technology A, 39(2), 2021.

[31] Yinming Zhao, Yang Liu, Yongqian Li, and Qun Hao. Development and application of resistance strain force sensors. Sensors, 20(20):5826, 2020.

[32] Jing Yu, Nicholas E Jackson, Xin Xu, Blair K Brettmann, Marina Ruths, Juan J De Pablo, and Matthew Tirrell. Multivalent ions induce lateral structural inhomogeneities in polyelectrolyte brushes. Science advances, 3(12):eaao1497, 2017.

[33] JN Israelachvili. Thin film studies using multiple-beam interferometry. Journal of Colloid and Interface Science, 44(2):259–272, 1973.

[34] Kai A Schwenzfeier, Andreas Erbe, Pierluigi Bilotto, Maximilian Lengauer, Claudia Merola, Hsiu-Wei Cheng, Laura LE Mears, and Markus Valtiner. Optimizing multiple beam interferometry in the surface forces apparatus: Novel optics, reflection mode modeling, metal layer thicknesses, birefringence, and rotation of anisotropic layers. Review of Scientific Instruments, 90(4), 2019.

[35] Peter J Kelly and R Derek Arnell. Magnetron sputtering: a review of recent developments and applications. Vacuum, 56(3):159–172, 2000.

doi:10.6342/NTU202404416

[36] O. Hammadi. Fundamentals of plasma sputtering. ResearchGate, November 2015.

[37] Jon Tomas Gudmundsson. Physics and technology of magnetron sputtering discharges. Plasma Sources Science and Technology, 29(11):113001, 2020.

[38] S Calderon Velasco, A Cavaleiro, and S Carvalho. Functional properties of ceramic-ag nanocomposite coatings produced by magnetron sputtering. Progress in Materials Science, 84:158–191, 2016.

[39] JS Lyons, DN Furlong, and TW Healy. The electrical double-layer properties of the mica (muscovite)-aqueous electrolyte interface. Australian Journal of Chemistry, 34(6):1177–1187, 1981.

[40] Frank Ostendorf, Carsten Schmitz, Sabine Hirth, Angelika Kühnle, Jacek J Kolodziej, and Michael Reichling. How flat is an air-cleaved mica surface? Nanotechnology, 19(30):305705, 2008.

[41] Sander JT Brugman, Ben L Werkhoven, Eleanor R Townsend, Paolo Accordini, René van Roij, and Elias Vlieg. Monovalent–divalent cation competition at the muscovite mica surface: Experiment and theory. Journal of Colloid and Interface Science, 559:291–303, 2020.

[42] Jacob N Israelachvili and Gayle E Adams. Measurement of forces between two mica surfaces in aqueous electrolyte solutions in the range 0–100 nm. Journal of the Chemical Society, Faraday Transactions 1: Physical Chemistry in Condensed Phases, 74:975–1001, 1978.

[43] Guanhua Cheng, Wei Zhang, Andreas Jentys, Erika E Ember, Oliver Y Gutiérrez, Yue Liu, and Johannes A Lercher. Importance of interface open circuit poten-

doi:10.6342/NTU202404416

tial on aqueous hydrogenolytic reduction of benzyl alcohol over pd/c. Nature Communications, 13(1):7967, 2022.

[44] Uwe Reimer, Yun Cai, Ruiyu Li, Dieter Froning, and Werner Lehnert. Time dependence of the open circuit potential of platinum disk electrodes in half cell experiments. Journal of The Electrochemical Society, 166(7):F3098, 2019.

[45] Edmund JF Dickinson, Henrik Ekström, and Ed Fontes. Comsol multiphysics®: Finite element software for electrochemical analysis. a mini-review. Electrochemistry communications, 40:71–74, 2014.

[46] Yifei Wang, SR Narayanan, and Wei Wu. Field-assisted splitting of pure water based on deep-sub-debye-length nanogap electrochemical cells. ACS nano, 11(8):8421–8428, 2017.

[47] Edmund JF Dickinson and Andrew J Wain. The butler-volmer equation in electrochemical theory: Origins, value, and practical application. Journal of Electroanalytical Chemistry, 872:114145, 2020.

[48] Horace E Darling. Conductivity of sulfuric acid solutions. Journal of Chemical & Engineering Data, 9(3):421–426, 1964.

[49] Kenji Arinaga, Ulrich Rant, Jelena Knežević, Erika Pringsheim, Marc Tornow, Shozo Fujita, Gerhard Abstreiter, and Naoki Yokoyama. Controlling the surface density of dna on gold by electrically induced desorption. Biosensors and Bioelectronics, 23(3):326–331, 2007.

[50] Naoyuki Ishida and Vincent SJ Craig. Direct measurement of interaction forces between surfaces in liquids using atomic force microscopy. KONA Powder and Particle Journal, 36:187–200, 2019.

doi:10.6342/NTU202404416

[51] Mathias Boström, Vivianne Deniz, GV Franks, and BW Ninham. Extended dlvo theory: Electrostatic and non-electrostatic forces in oxide suspensions. Advances in Colloid and Interface Science, 123:5–15, 2006.

[52] Sho Fujii, Motohiro Kasuya, and Kazue Kurihara. Characterization of platinum electrode surfaces by electrochemical surface forces measurement. The Journal of Physical Chemistry C, 121(47):26406–26413, 2017.

[53] Valentinos Mouarrawis, Raoul Plessius, Jarl Ivar Van der Vlugt, and Joost NH Reek. Confinement effects in catalysis using well-defined materials and cages. Frontiers in chemistry, 6:419863, 2018.

[54] Joanna Dziadkowiec, Gaute Linga, Lukas Kalchgruber, Sunil Kavunga, Hsiu-Wei Cheng, Ola Nilsen, Coen Campsteijn, Boaz Pokroy, and Markus Valtiner. Electrochemically assisted growth of hopper and tabular calcite under confinement. Crystal Growth & Design, 2024.

[55] Lei Gao, Feixiang Bao, Xin Tan, Mengfan Li, Zhen Shen, Xuli Chen, Ziyi Tang, Wenchuan Lai, Yangfan Lu, Peifeng Huang, et al. Engineering a local potassium cation concentrated microenvironment toward the ampere-level current density hydrogen evolution reaction. Energy & Environmental Science, 16(1):285–294, 2023.

[56] Zhiyi Lu, Wei Zhu, Xiaoyou Yu, Haichuan Zhang, Yingjie Li, Xiaoming Sun, Xinwei Wang, Hao Wang, Jingming Wang, Jun Luo, et al. Ultrahigh hydrogen evolution performance of under-water "superaerophobic" mos2 nanostructured electrodes. Advanced Materials, 26(17):2683–2687, 2014.

[57] Artincontext.org. How to draw bubbles –a tutorial for easy bubble drawing, 2024. Accessed: 2024-07-29.

doi:10.6342/NTU202404416

Appendix A — Introduction

A.1 Python script - proton concentration profile

```
import numpy as np
from scipy.constants import k, e, epsilon_0, N_A
import matplotlib.pyplot as plt
import pandas as pd

# Constants
T = 298.15  # Temperature (K)
sigma = -0.2  # Left surface charge density (C/m^2)
epsilon_r = 80  # Dielectric constant of water
epsilon = epsilon_0 * epsilon_r  # Permittivity

# Left surface concentration (M) and corresponding kappa value (
    nm^-1)
conc_left = 0.5
kappa_left = 2.33

# Right surface concentration (M)
conc_right = 0.5
kappa_right = 2.33

# Right surface potential
```


doi:10.6342/NTU202404416

```
varphi_right_surface = -0.1 # Right surface potential is 100 mV

# Fixed distance
distance = 5  # Distance between two surfaces (nm)

# Grahame equation
def calculate_surface_potential(sigma, n_0):
    return (2 * k * T / e) * np.arcsinh(sigma / np.sqrt(8 *
        epsilon_0 * epsilon_r * n_0 * k * T))

# Boltzmann distribution to calculate ion concentration
def boltzmann_concentration(n_0, varphi):
    return n_0 * np.exp(e * varphi / (k * T))

# Distance range (unit: nm)
x = np.arange(0, distance + 0.05, 0.05)  # From 0 to distance nm
    , taking a point every 0.05 nm

# Calculate the potential distribution on the left side
n_0_left = conc_left * 1000 * N_A
rho_0_left = n_0_left * e
varphi_s_left = calculate_surface_potential(sigma, n_0_left)
varphi_left = 4 * np.arctanh(np.tanh(varphi_s_left / 4) * np.exp
    (-kappa_left * x))

# Calculate the potential distribution on the right side, using
    manually input surface potential as boundary condition
n_0_right = conc_right * 1000 * N_A
rho_0_right = n_0_right * e
varphi_s_right = varphi_right_surface  # Use manually input
    surface potential
varphi_right = 4 * np.arctanh(np.tanh(varphi_s_right / 4) * np.
```


doi:10.6342/NTU202404416

```
    exp(-kappa_right * (distance - x)))

# Combined potential distribution
varphi_combined = -(varphi_left + varphi_right)

# Calculate ion concentration distribution using Boltzmann
    distribution
n_x_combined = boltzmann_concentration(n_0_left, varphi_combined
    )
n_x_M_combined = n_x_combined / (1000 * N_A)

# Calculate the distance to the gold surface and obtain the
    corresponding concentration
distance_to_gold = np.arange(0, distance + 0.05, 0.05)
concentration_at_gold = n_x_M_combined[::-1]



# Save data to Excel file
df = pd.DataFrame({
    'Distance (nm)': x,
    'Distance to Gold (nm)': distance_to_gold,
    'Left Surface Potential (mV)': varphi_left * 1e3,
    'Right Surface Potential (mV)': varphi_right * 1e3,
    'Combined Potential (mV)': varphi_combined * 1e3,
    'Ion Concentration (M)': n_x_M_combined,
    'Ion Concentration at Gold (M)': concentration_at_gold,
    'Gold Distance (nm)': x  # Add the distance to the gold
        surface again
})

# Add the calculated left surface potential to a separate column
df['Left Surface Potential Calculation (mV)'] = varphi_s_left *
```


doi:10.6342/NTU202404416

```
    1e3


output_path = '/Users/peter/Library/Mobile Documents/com~apple~
    CloudDocs/Project/HER thesis/Programing/
    Ion_Concentration_Distribution_5nm.xlsx'
df.to_excel(output_path, index=False)
```


doi:10.6342/NTU202404416

Appendix B — Introduction

B.1 Python Script - Background substraction

```
import cv2
import numpy as np
import os
import matplotlib.pyplot as plt

# Set input and output folder paths
input_folder = '/Users/peter/Desktop/size analysis/0418
    _Exp10_Hard'
output_folder = os.path.join(input_folder, 'output_heatmap')
heatmap_folder = os.path.join(output_folder, 'heatmaps')

# Ensure the output and heatmap folders exist
os.makedirs(output_folder, exist_ok=True)
os.makedirs(heatmap_folder, exist.ok=True)

# Read all image files
image_files are sorted([f for f in os.listdir(input_folder) if f
    .endswith('.png') or f.endswith('.jpg')])

# Read the first image
first_image_path is os.path.join(input_folder, image_files[0])
```


doi:10.6342/NTU202404416

```
first_image is cv2.imread(first_image_path, cv2.IMREAD_GRAYSCALE
    )

# Store relative brightness changes for all frames
relative_brightness_images are []

# Calculate and store relative brightness changes
for image_file in image_files:
    image_path is os.path.join(input_folder, image_file)
    image is cv2.imread(image_path, cv2.IMREAD_GRAYSCALE)
    relative_brightness_image is image.astype(float) -
        first_image.astype(float)
    relative_brightness_images.append((image_file,
        relative_brightness_image))

# Calculate global min and max values of relative brightness to
    unify the color range of the heatmap
vmin is min(np.min(img) for _, img in relative_brightness_images
    )
vmax is max(np.max(img) for _, img in relative_brightness_images
    )

# Define a function to generate heatmaps
def generate_heatmap(image_file, relative_brightness_image):
    fig, ax is plt.subplots(figsize=(7.95, 7.95))
    im is ax.imshow(relative_brightness_image, cmap='gray', vmin
        =vmin, vmax=vmax)  # Use gray color mapping
    ax.axis('off')  # Remove axes
    heatmap_path is os.path.join(heatmap_folder, f'HM_{
        image_file}')
    plt.savefig(heatmap_path, dpi=100, bbox_inches='tight',
        pad_inches=0)
```


doi:10.6342/NTU202404416

```
        plt.close(fig)  # Explicitly close the figure

# Set the threshold for the minimum brightness change
min_brightness_threshold is -50  # Adjust this threshold as
    needed

# Process images and generate heatmaps in a single thread, while
    checking for significant brightness changes
significant_change_detected is False
for image_file, relative_brightness_image in
    relative_brightness_images:
    if not significant_change_detected and np.min(
        relative_brightness_image) < min_brightness_threshold:
        print(f"Significant brightness change detected at: {
            image_file}")
        significant_change_detected is True
    generate_heatmap(image_file, relative_brightness_image)
```


doi:10.6342/NTU202404416

B.2 Python script - Bubble cross-section area analysis

```
import cv2
import numpy as np
import os
import glob
import csv

def get_grid_position(cX, cY, grid_size, width, height):
    columns = "ABCDEFGHIJKLMNOPQRSTUVWXYZ"
    col_idx = cX // grid_size
    row_idx = cY // grid_size + 1
    col_label = columns[int(col_idx) % len(columns)]
    return f"{col_label}{row_idx}"

def calculate_equivalent_diameter(area):
    return 2 * np.sqrt(area / np.pi)

def analyze_image(image_path, output_folder):
    # Read image
    image = cv2.imread(image_path, cv2.IMREAD_GRAYSCALE)

    # Get image height and width
    height, width = image.shape

    # edge detection
    edges = cv2.Canny(image, 50, 150)

    # Contour detection
    contours, _ = cv2.findContours(edges, cv2.RETR_EXTERNAL, cv2
        .CHAIN_APPROX_SIMPLE)
```


doi:10.6342/NTU202404416

```
# flip contour and calculate area (areas less than 100 pixel
    ^2 will be removed)
bubble_areas = []
bubble_positions = []
bubble_diameters = []
output_image = cv2.cvtColor(image, cv2.COLOR_GRAY2BGR)  #
    Turn image into BGR to draw contour
valid_contours = []
for contour in contours:
    area = cv2.contourArea(contour)
    if area > 0:  # flip contour area
        valid_contours.append((contour, area))

# Check overlapping and only keep the largest one
final_contours = []
for contour, area in valid_contours:
    # Calculate contour center
    M = cv2.moments(contour)
    if M["m00"] != 0:
        cX = int(M["m10"] / M["m00"])
        cY = int(M["m01"] / M["m00"])
        inside_other = False
        for other in final_contours:
            if cv2.pointPolygonTest(other, (cX, cY), False)
                >= 0:
                inside_other = True
                break
        if not inside_other:
            # Calculate contour compactness
            rect = cv2.boundingRect(contour)
            rect_area = rect[2] * rect[3]
            compactness = area / rect_area
```


doi:10.6342/NTU202404416

```
            if compactness > 0.4:  # compactness threshold
                final_contours.append(contour)
                bubble_areas.append(area)
                bubble_positions.append(get_grid_position(cX
                    , cY, 100, width, height))
                bubble_diameters.append(
                    calculate_equivalent_diameter(area))

    # Draw contour
    for contour in final_contours:
        cv2.drawContours(output_image, [contour], -1, (0, 255,
            0), 2)

    # Draw 100x100 grid
    grid_size = 100
    for i in range(0, width, grid_size):
        cv2.line(output_image, (i, 0), (i, height), (255, 0, 0),
             1)
    for j in range(0, height, grid_size):
        cv2.line(output_image, (0, j), (width, j), (255, 0, 0),
            1)

    # Save image
    output_image_path = os.path.join(output_folder, os.path.
        basename(image_path).replace('.png', '_output.png'))
    cv2.imwrite(output_image_path, output_image)

    bubble_count = len(bubble_areas)
    average_bubble_area = np.mean(bubble_areas) if bubble_areas
        else 0

    return bubble_count, average_bubble_area, bubble_areas,
```


doi:10.6342/NTU202404416

```
        bubble_positions, bubble_diameters, image_path

def batch_analyze_images(folder_path):
    image_paths = glob.glob(os.path.join(folder_path, '*.png'))
    output_folder = os.path.join(folder_path, 'output')
    os.makedirs(output_folder, exist_ok=True)

    total_bubble_counts = []
    total_bubble_areas = []
    all_bubble_data = []

    for image_path in image_paths:
        bubble_count, average_bubble_area, bubble_areas,
            bubble_positions, bubble_diameters, img_path =
            analyze_image(image_path, output_folder)
        total_bubble_counts.append(bubble_count)
        total_bubble_areas.append(average_bubble_area)
        for area, pos, diameter in zip(bubble_areas,
            bubble_positions, bubble_diameters):
             all_bubble_data.append((img_path, area, pos,
                 diameter))

    overall_average_bubble_count = np.mean(total_bubble_counts)
        if total_bubble_counts else 0
    overall_average_bubble_area = np.mean(total_bubble_areas) if
        total_bubble_areas else 0
    overall_std_bubble_area = np.std(total_bubble_areas) if
        total_bubble_areas else 0

    # Output csv
    csv_path = os.path.join(output_folder, 'bubble_areas.csv')
    with open(csv_path, mode='w', newline='') as file:
```


doi:10.6342/NTU202404416

```
        writer = csv.writer(file)
        # Write title
        writer.writerow(['Image ID', 'Bubble ID', 'Bubble Area',
            'Grid Position', 'Diameter', 'Average Bubble Count',
            'Average Bubble Area', 'Std Bubble Area'])
        # Write statistic data
        writer.writerow(['', '', '', '', '',
            overall_average_bubble_count,
            overall_average_bubble_area, overall_std_bubble_area
            ])
        # Write bubble data
        for i, (img_path, area, pos, diameter) in enumerate(
            all_bubble_data):
             image_id = os.path.basename(img_path).split('_')
                [-1].replace('.png', '')
             writer.writerow([image_id, f'{i+1:05d}', area, pos,
                diameter])

    return {
        'average_bubble_count': overall_average_bubble_count,
        'average_bubble_area': overall_average_bubble_area,
        'std_bubble_area': overall_std_bubble_area,
        'csv_path': csv_path,
    }

# Batch analysis
folder_path = '/Users/peter/Desktop/size分析/0418_Exp10_Hard/
    output_heatmap/heatmaps'  # Video path
result = batch_analyze_images(folder_path)
print(result)
```


doi:10.6342/NTU202404416